JGR Solid Earth

RESEARCH ARTICLE
10.1029/2021JB022942

New Constraints for the On-Shore Makran Subduction Zone Crustal Structure

Keith Priestley[1], Farhad Sobouti[2], Rahil Mokhtarzadeh[2], Mohsen A. Irandoust[2], Reza Ghods[2], Khalil Motaghi[2], and Tak Ho[1]

[1]Bullard Laboratories, University of Cambridge, Cambridge, UK, [2]Department of Earth Sciences, Institute for Advanced Studies in Basic Sciences (IASBS), Zanjan, Iran

Key Points:

- Due to past logistical constraints and low seismicity, little is known of the on-shore structure of the Makran Subduction Zone
- Analysis shows a normal oceanic crust near the coast which transforms to eclogite at deeper depths, and a flat continental Moho to the north
- The peridotite of the mantle wedge is ~20% serpentinized and the high V_p/V_s ratio observed may result from ~1%–2% partial melt

Supporting Information:

Supporting Information may be found in the online version of this article.

Correspondence to:

K. Priestley,
kfp10@cam.ac.uk

Citation:

Priestley, K., Sobouti, F., Mokhtarzadeh, R., Irandoust, M. A., Ghods, R., Motaghi, K., & Ho, T. (2022). New constraints for the on-shore Makran subduction zone crustal structure. *Journal of Geophysical Research: Solid Earth*, *127*, e2021JB022942. https://doi.org/10.1029/2021JB022942

Received 3 AUG 2021
Accepted 8 DEC 2021

Author Contributions:

Conceptualization: Keith Priestley, Farhad Sobouti
Data curation: Farhad Sobouti, Rahil Mokhtarzadeh, Reza Ghods, Khalil Motaghi
Formal analysis: Keith Priestley, Rahil Mokhtarzadeh, Mohsen A. Irandoust, Tak Ho
Methodology: Keith Priestley
Software: Tak Ho
Writing – original draft: Keith Priestley

Abstract The Makran Subduction Zone is the primary seismic/tsunami hazard of the northwestern Indian Ocean, but little is known of its on-shore seismic structure. We derived a shear wave velocity model extending to >100 km depth beneath a ~400 km-long seismic profile oriented parallel to the convergence vector of the Arabian Sea Plate. Receiver function/surface wave analysis shows that the average structure in the coastal region comprises a ~22–28 km-thick low wavespeed sedimentary cover and a 6–8 km-thick gradient zone overlying >100 km-thick high wavespeed upper mantle. The ocean-basement interface dips gently northward, remaining a positive impedance contrast to ~50 km depth at ~250 km north of the coast where it disappears as the basaltic/gabbroic oceanic crust has probably transformed to eclogite. Further north, a weak arrival at ~5 s in the receiver functions appears, grading northward into the Moho arrival of the continental Iranian Plateau. This disruption in the seismic signature of the Moho occurs in the forearc region where the dip of the subducting oceanic plate steepens. The southern Iranian Plateau's continental crust has an average V_s of 3.55 ± 0.05 km s^{-1}, an almost flat Moho 40–45 km deep, and a sub-Moho mantle V_s of 3.75 ± 0.05 km s^{-1} in the 50–80 km depth range. Weak Moho conversions probably result from ~20% serpentinization of peridotite in the mantle wedge. Receiver functions indicate a flat continental Moho – no crustal root beneath the high topography region of the volcanic belt, which therefore must be compensated by low upper mantle densities. The high V_p/V_s ratio observed for the mantle wedge suggests ~1%–2% partial melt.

Plain Language Summary The Makran Subduction Zone is the primary seismic/tsunami hazard of the northwestern Indian Ocean, but little is known of its on-shore structure. Although earthquake rates in the Makran are generally low, there have been historic destructive earthquakes accompanied by tsunamis. The poor knowledge of the Makran structure makes it difficult to evaluate the seismic and tsunami potential. From mid-2016 to late 2020 we operated seismic stations along a ~400 km-long profile crossing the Makran Subduction Zone. Our analysis shows a shallow-dipping oceanic crust beneath thick sediments near the coast. To the north, there is a normal continental crust, but the underlying mantle has a very low velocity. In the transition region, the seismic signature is disrupted in the forearc region where the dip of the subducting oceanic plate steepens. Weak Moho conversions probably result from ~20% serpentinization of peridotite in the mantle wedge. Receiver functions indicate a flat continental Moho – no crustal root beneath the high topography region of the volcanic belt, which therefore must be supported by low upper mantle densities. The low V_s compared to the V_p observed for the mantle wedge suggests ~1%–2% partial melt.

1. Introduction

The Makran Subduction Zone (Figure 1), which extends ~1,000 km from the Strait of Hormuz in the west to Sonmiani Bay near Karachi in the east, results from the ongoing northward subduction of the Arabian Sea Plate beneath southeastern Iran and southwestern Pakistan. It is characterized by a shallow, gently-dipping subduction interface (e.g., Kopp et al., 2000; Smith et al., 2012), a high sedimentation rate (e.g., Ellouz-Zimmermann, Deville, et al., 2007; McCall, 1997), an extremely broad accretionary prism which is largely sub-aerial and no bathymetric trench. While great historic earthquakes (e.g., Byrne et al., 1992) accompanied by tsunamis (e.g., Hoffmann et al., 2013) have occurred on the Makran Subduction Zone, in general, seismicity is low, especially in the western Makran (e.g., Engdahl et al., 2006). A number of studies have focused on the structure of the offshore Makran accretionary prism (e.g., Kopp et al., 2000; Smith et al., 2012) and teleseismic tomographic studies show a high-velocity, steep northward-dipping feature in the upper mantle beneath southern Iran and Pakistan (e.g., Van der Meer et al., 2018). However, although the Makran Subduction Zone is the primary seismological

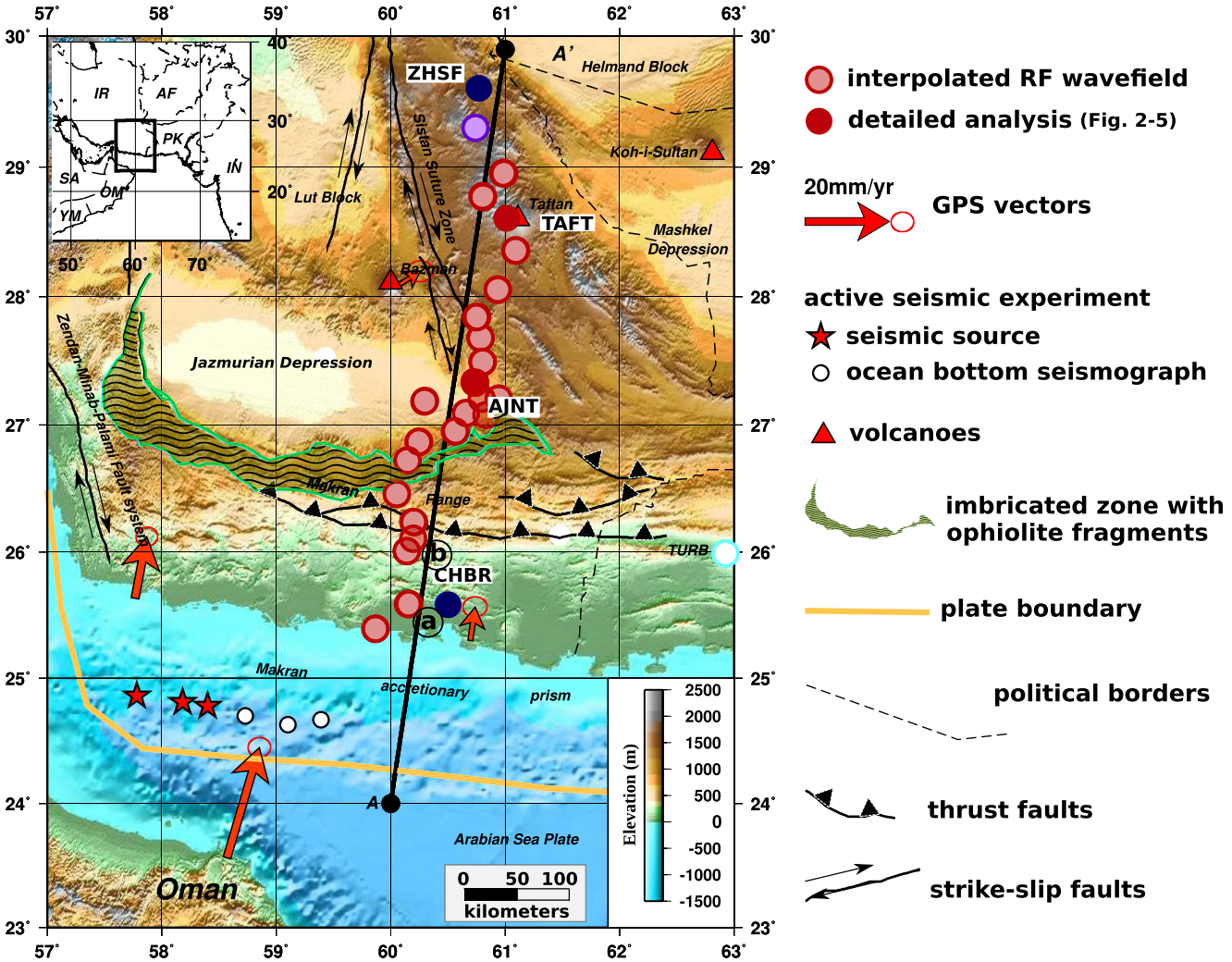

Figure 1. Summary map of the topographic and tectonic features of the western Makran region and the locations of seismographs providing data for this study. The location of the western Makran in the wider Middle East region is shown in the inset map in the upper left-hand corner of the figure. Seismograph sites are indicated by circles where the color indicates the source of the data – red IASBS/CAM, blue INSN and purple IRSC stations. The solid red and blue circles indicate the locations of the four sites whose receiver functions and group velocity curves are discussed in detail in Section 4 (Figures 2–5), while the lightly-filled and solid circles designate sites whose receiver functions are used to form the receiver function interpolated wavefield image in Figure 6. The light blue circle labeled TURB denotes the location of the Pakistan station discussed in Penney et al. (2017). Large red arrows indicate the GPS horizontal velocities and their 95% confidence ellipses in the Eurasia-fixed reference frame for the period 1999–2001 (Vernant, Nilforoushan, Hatzfeld, et al., 2004). The fault locations are taken from Walker et al. (2010). The light green shaded area shows the region of the imbricated zone with ophiolite fragments (Ghazi et al., 2004). The red stars and white circles in the off-shore western Makran accretionary prism show the locations of the explosions and OBS instruments, respectively, of Niazi et al. (1980). The line AA' denotes the location of the receiver function profile shown in Figure 6. The open circles labeled a and b indicate the locations of the velocity models shown in Figure 8. Abbreviations in the inset map: IR, Iran; AF, Afghanistan; PK, Pakistan; IN, India; SA, Saudi Arabia; OM, Oman and YM, Yemen.

hazard of the western Indian Ocean, few details of its shallow structure are known. Past logistical constraints in southern Iran and Pakistan have made field work problematic and, due to the low level of seismicity, the shallow subduction zone has been difficult to map teleseismically. Improved knowledge of the Makran Subduction Zone structure is a prerequisite in evaluating its tsunami potential.

In this paper, we present a model for the shallow shear wave (V_s) structure of the western Makran Subduction Zone derived from the analysis of seismic data acquired from a portable seismic network we have operated in this region in 2016–2020, as well as recordings from three permanent seismic stations. In Section 2, we briefly summarize the tectonic setting and past seismological studies for the western Makran; Section 3 outlines the data source and the analysis methodology; Section 4 describes the V_s model resulting from our data analysis and Section 5 discusses the geophysical and geologic processes occurring in the Makran Subduction Zone in light of

our structural model. An important aspect of our study is that the Makran Subduction Zone is the only subduction zone where land seismographs can be located above a substantial portion of the subducting plate in the forearc region.

2. Tectonic Setting and Results of Previous Work

The Arabian Sea Plate (Figure 1), the last remnant of the Neo-Tethys, is presently subducting roughly northward beneath the coast of southern Iran and Pakistan. Plate reconstructions imply that the convergence rate increases from 3.7 cm yr^{-1} in the western Makran to 4.2 cm yr^{-1} in the eastern Makran (DeMets et al., 1990), but GPS measurements estimate the present convergence rate of the western Makran to be only 2.7 cm yr^{-1} (Khorrami et al., 2019; Vernant, Nilforoushan, Hatzfeld, et al., 2004). In the west, the Makran is separated from the Arabian-Eurasian continental collision zone in the Zagros by the right-lateral Zendan-Minab-Palami Fault system (Figure 1) and in the east from the Indo-Eurasian continental collision zone by the left-lateral Ornach-Nal-Chaman Fault system (to the east of the area shown in Figure 1). The Zendan-Minab-Palami Fault system experiences a low level of seismicity (Yamini-Fard et al., 2007) and does not appear to be a major through-going lithospheric fault system. Instead, it is a localized transition zone accommodating the differential motion between the Zagros and Makran (Gholamzadeh et al., 2009). The western Makran experiences a lower level of seismicity than does the eastern Makran (Byrne et al., 1992) and a short-duration deployment of ocean bottom seismometers to the south of the western Makran recorded no earthquakes (Niazi et al., 1980).

Subduction beneath the Makran probably started during Late Cretaceous time (Arthurton et al., 1982; Dykstra & Birnie, 1979). The age of the presently-subducting oceanic crust of the Arabian Sea Plate is not well determined due to a lack of seafloor magnetic anomalies, but it is probably of Jurassic or Cretaceous age (e.g., Hutchison et al., 1981; McKenzie & Sclater, 1971). The accretionary prism (Figure 1) is more than 350 km wide with only the frontal 100–150 km currently submarine. The topography of the accretionary wedge varies from ~3,000 m below sea level to ~1,500 m above sea level; however, there is no bathymetric trench. Most of the north-south convergence is absorbed in the subduction of the Arabian seafloor; however, a small amount of shortening has been observed between the Makran coast and the volcanic arc ~250 km to the north (Khorrami et al., 2019; Vernant, Nilforoushan, Chery, et al., 2004). The shortening within the on-shore portion of the accretionary prism may contribute to the uplift of ~0.2 mm yr^{-1} (Reyss et al., 1999). The prism contains extensive zones of Mesozoic age melange and large intact ophiolite (Figure 1) (Ghazi et al., 2004). To the north of the Makran accretionary prism lies the subduction-related Jazmurian and Mashkel Depressions (Figure 1), and further north lies a sub-parallel andesitic-to-rhyolitic volcanic arc (Figure 1) with the prominent centers of Bazman, Taftan and Koh-i-Sultan (Farhoudi & Karig, 1977).

The off-shore seismic structure of the Makran accretionary prism has been studied extensively (e.g., Fowler et al., 1985; Grando & McClay, 2007; Kopp et al., 2000; Kukowski et al., 2001; Niazi et al., 1980; Smith et al., 2012). However, there have been only a few seismological studies of the on-shore structure and they reach conflicting conclusions. Al-Lazki et al. (2014) found that a very low P_n velocity (<7.7 km s^{-1}) beneath the western Makran and low P_n wavespeed (~7.9 km s^{-1}) extends to the north of the Jazmurian Depression and the volcanic arc. Several surface wave studies covered portions of the Makran, but all have poor path coverage. The partitioned surface waveform tomography of Shad Manaman et al. (2011) depicts a shallow, high-wavespeed feature extending from beneath the Arabian seafloor to below the coastal region of the Makran and then dipping northward to about 250 km below central Iran. The ambient noise Rayleigh wave (16–40 s period) group velocity tomography of Abdetedal et al. (2015) found that the Mohorovičić discontinuity (Moho) beneath the Makran deepened from less than 25 km in the coastal region to more than 50 km beneath the volcanic arc. Abdollahi et al. (2018) inverted the Abdetedal et al. (2015) dispersion data jointly with free-air gravity data, finding that the crust varied from an average V_s ~3.95 km s^{-1} and ~33 km thick near the coast to an average V_s ~3.75 km s^{-1} and ~48 km thick beneath the volcanic arc. There are three published receiver function results for CHBR (Figure 1). Taghizadeh-Farahmand et al. (2015) used HK-stacking and forward modeling and found the crust to be ~33 ± 2 km thick with a V_p/V_s of ~1.77. Penney et al. (2017) inverted the CHBR receiver function with a Rayleigh wave group velocity and found a low V_s ~3 km s^{-1}, 26 ± 2 km-thick layer, which they suggested were sediments of the accretionary wedge, overlying a ~4.1 km s^{-1} oceanic basement. Penney et al. (2017) found a similar structure below the TURB (Figure 1) in the Makran of southwestern Pakistan. Motaghi et al. (2020) used HK-stacking and forward modeling of receiver functions from recordings at CHBR and nearby stations, concluding that the sediments were as much as

Table 1
Makran Seismic Profile Station Parameters – The Moho at Sites AJNT, KAHN, TAFT and KALL is Uncertain or Unclear and There May Not be a Distinct Moho

Net	Sta	Lat (°N)	Lon (°E)	Elv (m)	Number RFs	Moho (km)	Crust $<V_s$ km s$^{-1}>$	Upper mantle $<V_s$ km s$^{-1}>$
C5	AZIZ	25.387	59.886	9	24	41 (4)	3.36 (0.01)	4.36 (0.01)
C5	KAHR	25.597	60.146	28	30	36 (4)	3.18 (0.01)	4.34 (0.01)
I2	CHBR	25.595	60.482	125	308	28 (2)	2.94 (0.01)	4.17 (0.01)
C5	RAMZ	25.990	60.137	244	85	30 (2)	3.05 (0.01)	4.39 (0.01)
C5	JALA	26.160	60.182	378	26	34 (2)	3.21 (0.02)	4.49 (0.02)
C5	HITA	26.254	60.160	481	42	36 (2)	3.20 (0.02)	4.46 (0.02)
C5	MALK	26.451	60.051	844	119	37 (2)	3.22 (0.01)	4.40 (0.02)
C5	GORD	26.715	60.154	922	69	44 (4)	3,36 (0.01)	4.39 (0.01)
C5	SEIF	26.872	60.232	742	53	46 (2)	3.35 (0.02)	4.32 (0.02)
C5	BAZZ	26.947	60.562	804	29	51 (2)	3.42 (0.01)	4.39 (0.01)
C5	BAND	26.949	60.967	1,103	34	51 (2)	3.47 (0.1)	4.39 (0.01)
C5	KHIR	27.077	60.663	575	41	52 (6)	3.47 (0.02)	4.37 (0.01)
C5	SAID	27.165	60.380	500	99	54 (2)	3.51 (0.01)	4.31 (0.01)
C5	GANJ	27.213	60.938	779	46	53 (2)	3.40 (0.01)	4.12 (0.01)
C5	GHAD	27.323	60.781	686	37	53 (2)	3.33 (0.01)	4.15 (0.01)
C5	AJNT	27.330	60.740	681	92	59 ?	3.35 (0.01)	4.09 (0.01)
C5	KAHN	27.489	60.823	823	46	55 ?	3.30 (0.01)	3.99 (0.02)
C5	KOOG	27.684	60.782	988	22	50 (4)	3.23 (0.01)	3.92 (0.01)
C5	KARV	27.835	60.765	1,204	58	49 (2)	3.25 (0.01)	3.88 (0.01)
C5	HABI	28.061	60.936	1,394	34	47 (2)	3.18 (0.01)	3.78 (0.01)
C5	NMAT	28.363	61.085	1,560	91	49 (4)	3.12 (0.02)	3.69 (0.01)
C5	TAFT	28.598	61.029	2267	209	57 ?	3.16 (0.01)	3.69 (0.01)
C5	KALL	28.775	60.820	2144	43	?	3.32 (0.03)	3.92 (0.02)
C5	JOON	28.948	60.987	1,724	190	43 (4)	3.21 (0.01)	3.75 (0.02)
IR	ZHDN	29.399	60.810	1,511	137	48 (2)	3.48 (0.01)	4.13 (0.02)
I2	ZHSF	29.611	60.775	1,575	518	42 (2)	3.41 (0.01)	3.95 (0.01)

Note. For networks: C5, IASBS/CAM; I2, INSN; IR, IRSC.

20 km thick beneath the coastal plain and overlay a 4.5–7 km-thick oceanic crust. Haberland et al. (2021) present a *P*-wave model for the on-shore structure of the accretionary prism from wide-angle seismic recordings. We discuss these published results in more detail in Section 5.

3. Data Source and Analysis

3.1. Data

The crust and uppermost mantle structure of the western Makran presented in this paper is derived from the analysis of teleseismic body-wave and local and regional surface wave recordings. These seismic recordings come primarily from a network of 23 temporary seismographs we operated between mid-2016 and late 2020 over the western portion of the Makran Subduction Zone in southern Iran (IASBS/CAM – red-outlined circles in Figure 1). In addition to using data from the temporary network, we include data from two seismographs operated by the International Institute of Earthquake Engineering and Seismology (INSN – blue circles, Figure 1) and one seismograph operated by the University of Tehran (IRSC – purple circles, Figure 1). Details of the profile stations are given in Table 1. The 26 recording sites lie along a ~400 km long profile, trending approximately northward

from the coast more or less parallel to the plate convergence direction and with an average of ~20–25 km station spacing. There is some deviation from a strict linear profile due to access and security constraints.

The fundamental mode group velocity dispersion observations for the western Makran are taken from the work of Ahmadzadeh-Irandoust et al. (2022). They used multiple-filter analysis (Dziewonski et al., 1969) to extract longer period ($\gtrapprox$15 s) dispersion information from vertical component seismograms of magnitude 4 and greater earthquakes recorded on Iranian seismographs, including the Makran stations. Their short period dispersion was determined from ambient noise analysis (Bensen et al., 2007) from the Makran network recordings. Ahmadzadeh-Irandoust et al. (2022) merged their dispersion measurements with those of Gilligan and Priestley (2018). They then employed the procedure of Debayle and Sambridge (2004) to invert path-average surface wave measurements on a $1° \times 1°$ grid at sixteen periods between 5 and 70 s to obtain the geographic variation of the group velocity. We interpolated these dispersion maps to build 5–70 s pseudo-dispersion curves for each Makran network recording site.

3.2. Methodology

Teleseismic receiver function analysis (Burdick & Langston, 1977; Phinney, 1964; Langston, 1977) is now an established seismological tool for determining the V_s and V_p/V_s structure beneath a seismograph site, and we apply this technique to determine the V_s structure beneath the on-shore portion of profile AA' (Figure 1). The waveforms from events greater than m_b 5.5 in the distance 30°–90° were band-pass filtered between 0.05 and 2.0 Hz, rotated from NS and EW to radial and transverse with respect to the event-station great-circle path, and receiver functions were computed using the iterative deconvolution method of Ligorria and Ammon (1999). To stabilize the time domain deconvolution, we applied a 2.5 Gaussian width filter (corner frequency ~1.0 Hz) in the deconvolution. In addition, we computed receiver functions for each event using several different Gaussian filters (1.0, 1.6, 2.5, 3.5, 4, 5) to examine the variations in crustal response with frequency, but the Gaussian 2.5 receiver functions are the main focus of our analysis in this paper. To examine the backazimuth variation we form backazimuthal gathers for radial and transverse receiver functions after correcting for moveout (e.g., Figure 2a). The moveout-corrected receiver functions are then stacked to determine a mean site receiver function with error bounds (e.g., Figure 2b).

We then invert the mean site receiver function jointly with the pseudo-dispersion curve for each site using the linearized least-squares inversion algorithm of Herrmann (2013). Receiver functions are sensitive to high wave-number features beneath the recording location and do not provide strong constraints on the absolute wavespeed. Surface wave dispersion constrains the absolute wavespeed in a broad region surrounding the recording site but has a low sensitivity to discontinuities. The starting inversion model consisted of a finely parameterized structure defined by 2 km-thick flat-lying isotropic layers with S-velocity and V_p/V_s for each layer and extending to 280 km depth. The wavespeed of the model used in the inversion (e.g., Figure 2d) is based on the velocity model AK135 (Kennett et al., 1995) but with the crustal wavespeeds replaced by the uppermost mantle wavespeed of AK135 (4.48 km s^{-1} to 110 km depth). Since there is no a priori crustal model imposed, the inversion procedure will introduce layering as required by the data. We repeated the inversion by replacing the shallow structure with velocities of 4.28 and 4.68 km s^{-1} to examine the effect of the starting model on the outcome and for both of these, the resulting inversion model converged to the model found from the 4.48 km s^{-1} starting model. The receiver functions are given a higher weight (87.5%) compared to the surface waves (12.5%) in the inversion.

For the four representative recording sites whose results are shown in Figures 2–5), we first simplified the inversion model by combining similar adjacent 2-km-thick layers into thicker structures with either constant V_s or constant V_s-gradient to form a minimum parameter model which explained the data. We then tested the main features of the simplified model to evaluate their importance in fitting the data.

Thus, our underlying assumptions are that the structure beneath each seismograph site is close to one-dimensional (1-D), can be approximated by plane isotropic layers, and that the effect of side scattering from local crustal heterogeneity is minimal. Receiver function analysis normally assumes simple horizontal layering with the velocity changing only in the vertical dimension. Subduction zone environments can be significantly more complex due to dipping structures; however, a number of studies (e.g., Ferris et al., 2003; Owens et al., 1988; Yuan et al., 2000) have shown that the dipping structures can be successfully modeled in subduction zone environments using receiver function analysis. In this study, we do not attempt to reproduce all of the signal in each receiver function,

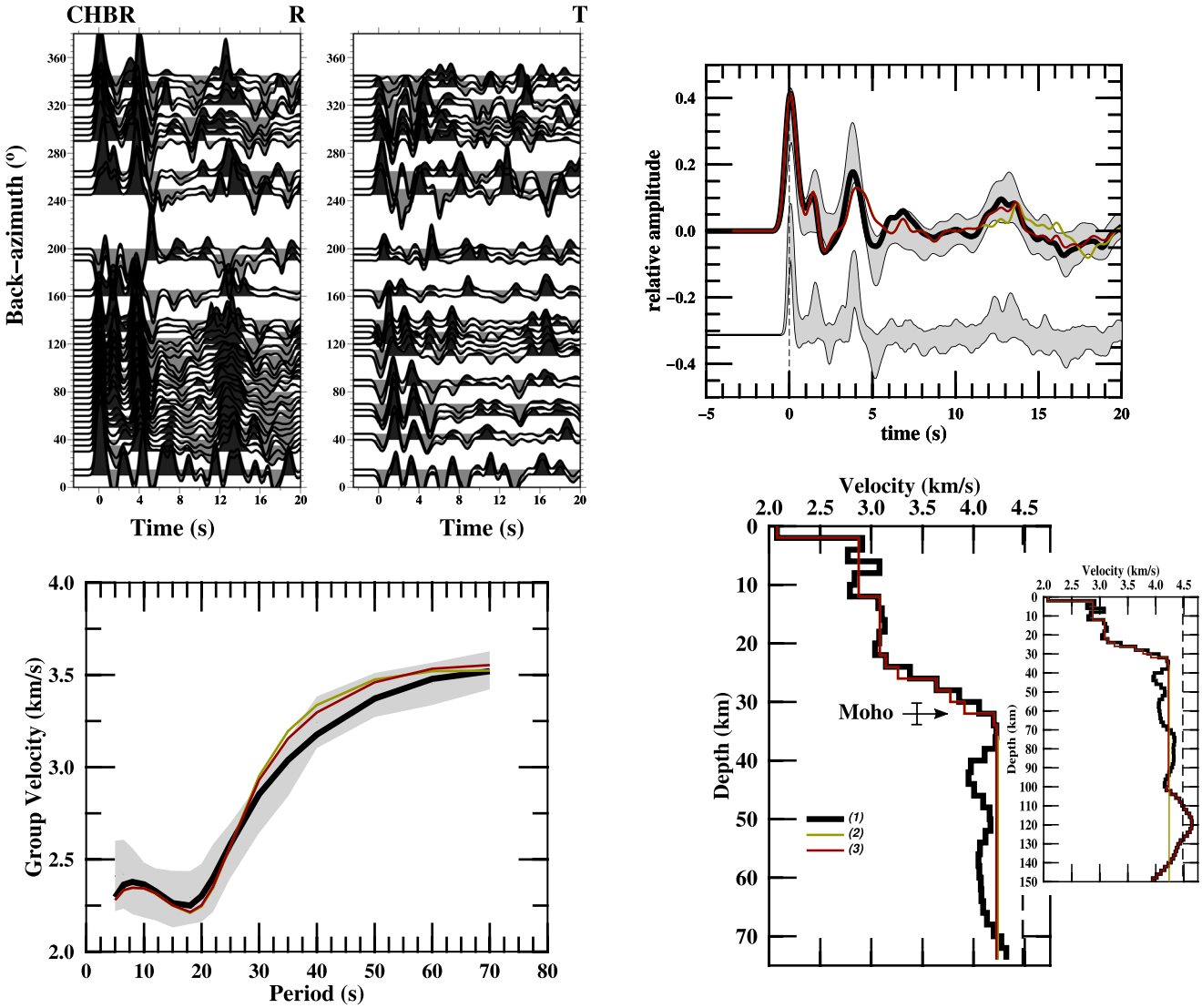

Figure 2. Summary of CHBR (Figure 1) teleseismic receiver functions and surface wave data and their analysis. (a) The radial (left panel) and tangential (right panel) receiver function backazimuth gathers in 5° bins. (b) The ±1-standard deviation bounds of the CHBR radial receiver function are displayed as the gray bands. The upper receiver function is smoothed with a 2.5 Gaussian and is used in the determination of the V_s (z) model in (d), and the lower receiver function is smoothed with a 5.0 Gaussian. Plotted over the 2.5 Gaussian receiver function bounds are the synthetic receiver functions computed for the inversion V_s model (solid black line), the simplified model (red line) and forward sensitivity test model (green lines) shown in (d). (c) The ±1-standard deviation bounds of the CHBR fundamental mode group velocity pseudo-dispersion derived from the tomographic maps of Ahmadzadeh-Irandoust et al. (2022) are displayed as the gray band; over these are plotted synthetic Rayleigh wave group dispersion curves computed for the inversion model, the simplified model and for the forward sensitivity test model. In (d), V_s (z) models for the crust and uppermost mantle beneath CHBR: (1) model derived from inverting the CHBR mean receiver function and pseudo-dispersion data; (2) simplified model; and (3) effect of removing the velocity increase beginning at ∼100 km depth. The long-dashed black line is the inversion starting model. The V_s (z) structure to 150 km depth is shown in the inset of (d). We identify the Moho as a significant break in slope of V_s (z) where V_s first is very close to or exceeds 4.0 km s^{-1}. This is a clear transition for all sites except those marked with a "?" in Table 1.

but we create a simple model for the on-shore portion of the Makran Subduction Zone which explains the stable features in the observed receiver functions and is consistent with other geophysical and geological observations.

The difference in spatial resolution of the receiver functions and surface wave dispersion suggests that we interpolate the receiver function wavefield to equalize the lateral sensitivity of the two data sets and simplify the complexity in the receiver functions. Following Chai et al. (2015), we interpolated the receiver functions recorded along the profile to acquire the interpolated receiver function wavefield. The moveout-corrected receiver functions were weighted and stacked with the receiver functions within ±20 km of the interpolated point weighted unity and with the weight linearly decreasing to zero between 20–80 km from the interpolation point.

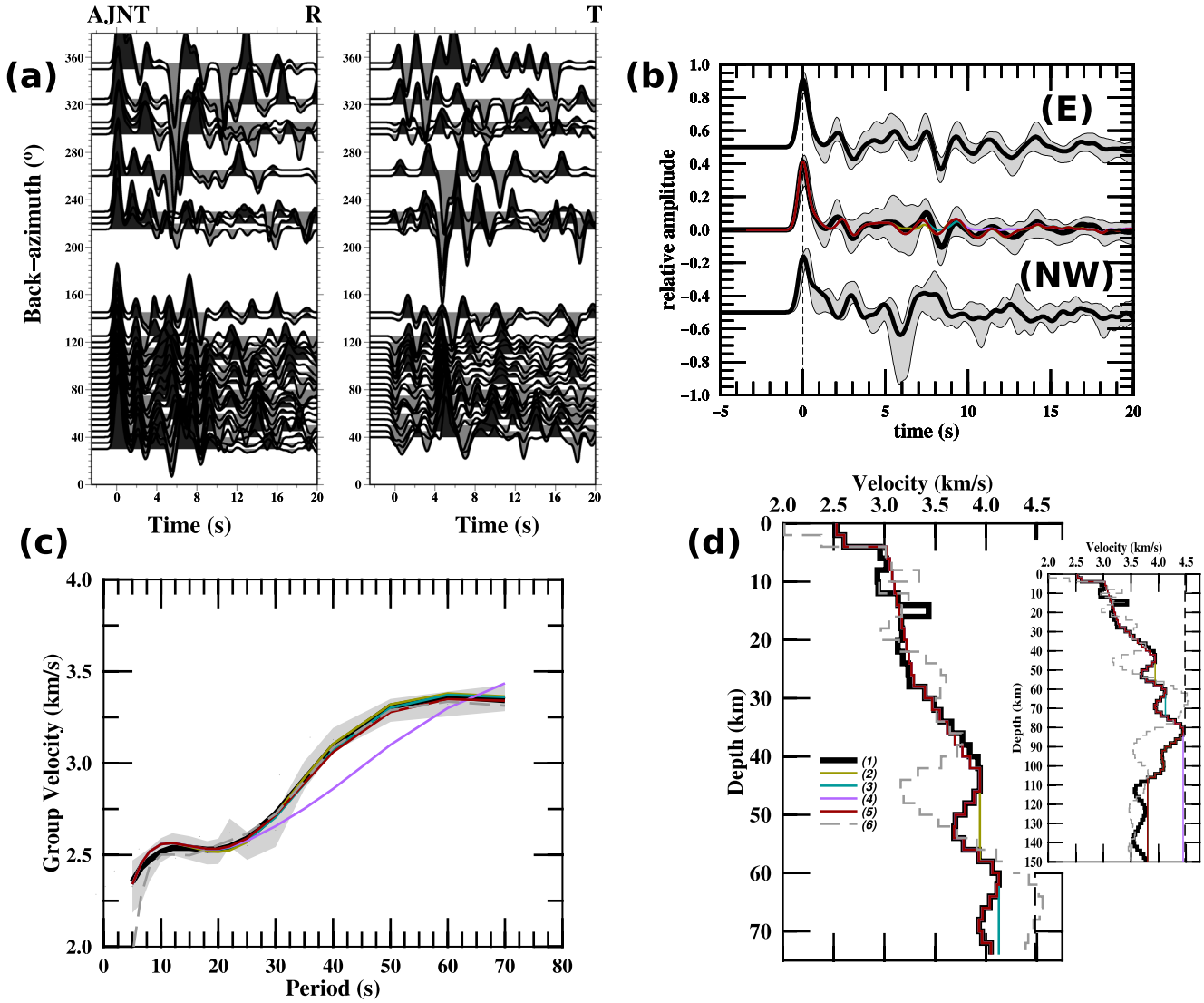

Figure 3. Summary of the AJNT (Figure 1) teleseismic receiver functions and surface wave data and their analysis. The figure format is similar to that of Figure 2 except for (b) where, in addition to the mean stacked 2.5 Gaussian radial receiver function, stacked radial receiver functions for eastern (upper trace) and northwestern (lower trace) backazimuths are included. In (d), V_s (z) models for the crust and uppermost mantle beneath AJNT: (1) V_s model derived from inverting the mean receiver function and pseudo-dispersion data; (2) simplified model; (3) effect of removing the LVZ centered at ~52 km depth; (4) effect of removing the LVZ centered at ~68 km depth; (5) effect of removing the LVZ below ~80 km; and (6) model derived from inversion of the northwestern backazimuth receiver function and pseudo-dispersion data. The dashed black line is the inversion starting model.

4. Seismic Structure of the Makran Subduction Zone

The receiver functions and Rayleigh wave group velocity dispersion curves fall into three broad spatial groupings along the profile – those from the coastal sites on the thick sediments of the Makran Accretionary Prism extending from the coast northward to the Makran Range, those from sites across the eastern edge of the Jazmurian Depression Basin in the central part of the profile, and those from sites crossing the Sistan Suture Zone on the Iranian Plateau at the northern end of the profile. The Makran Volcanic Arc crosses the Sistan Suture Zone. In this section, we discuss details of the analysis for data from representative sites from each of these regions. Results for the remaining sites are summarized in Table 1.

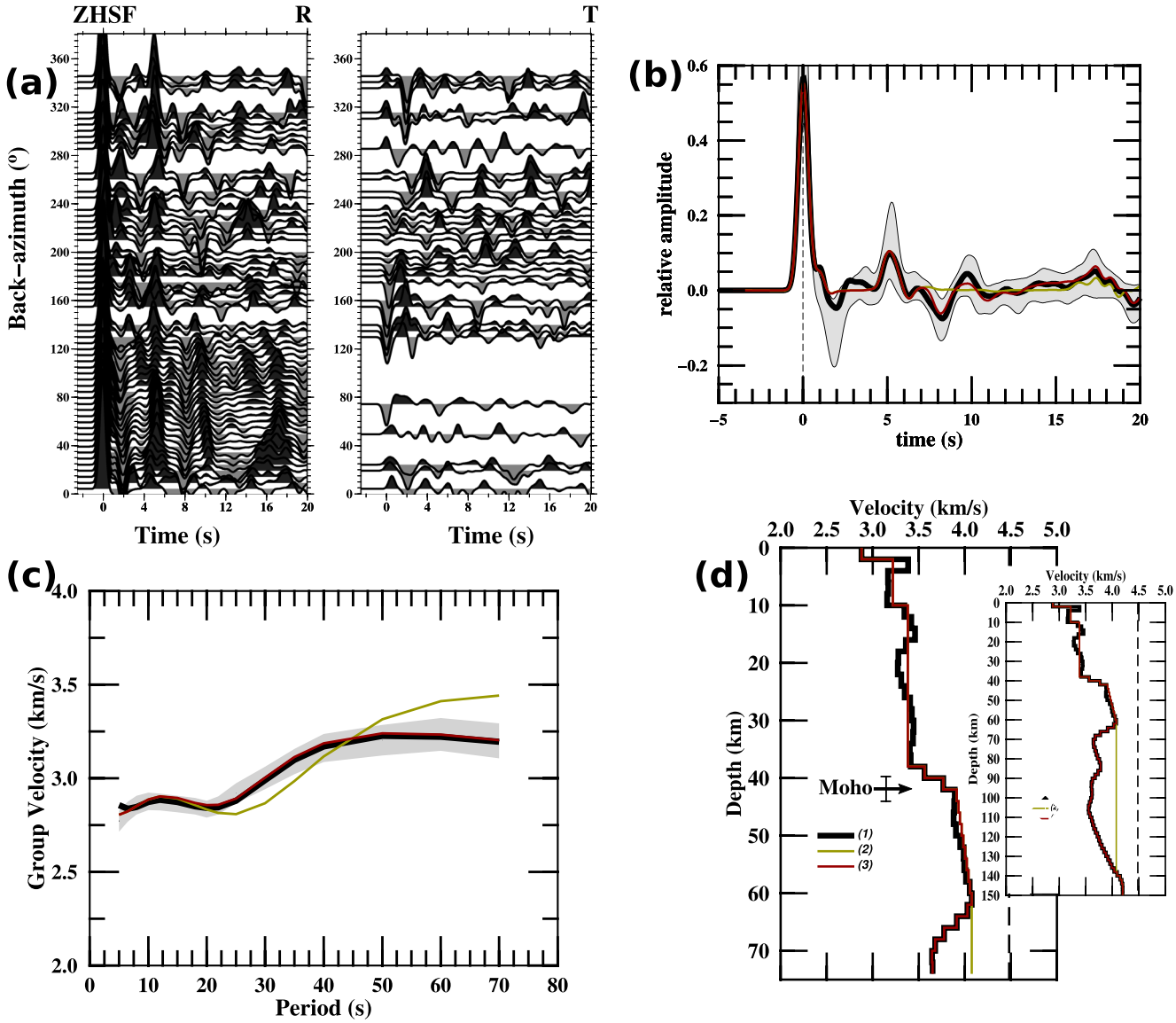

Figure 4. Summary of the ZHSF (Figure 1) teleseismic receiver functions and surface wave data and analysis. The figure format is similar to Figure 2 but shows only the mean 2.5 Gaussian receiver function in (b). In (d), V_s (z) models for the crust and uppermost mantle beneath ZHSF: (1) V_s model derived from inverting the mean receiver function and pseudo-dispersion data; (2) simplified model; and (3) effect of removing the LVZ below 60 km depth. The dashed black line is the inversion starting model.

4.1. The On-Shore Makran Accretionary Prism

The on-shore coastal plain of the Makran is separated from the off-shore portion of the accretionary prism by a narrow coastal strip where normal faults and mud volcanoes are prominent (e.g., Back & Morley, 2016; Von Rad et al., 2000). In the coastal plain, the surface geology consists primarily of thick sequences of relatively homogeneous slope and shelf facies rocks which have experienced ~20%–30% shortening with broad synclines up to 20 km across, separated by tighter thrusted anticlines. Further inland, in the central Coast Ranges, only turbidites are exposed. These have been tightly folded and imbricated, with shortening strains of 60% or more (Platt et al., 1985).

The recordings from the permanent station CHBR (Figure 1) are representative of the data from the temporary coastal sites, but the CHBR data are much more numerous. The receiver function *vs*. backazimuth observed at CHBR (Figure 2a) shows that over most backazimuths, there is a strong arrival at ~4 s. In the 70–260° backazimuth range (all backazimuth ranges are clockwise from north), there is a significant phase at ~2 s, and a broad

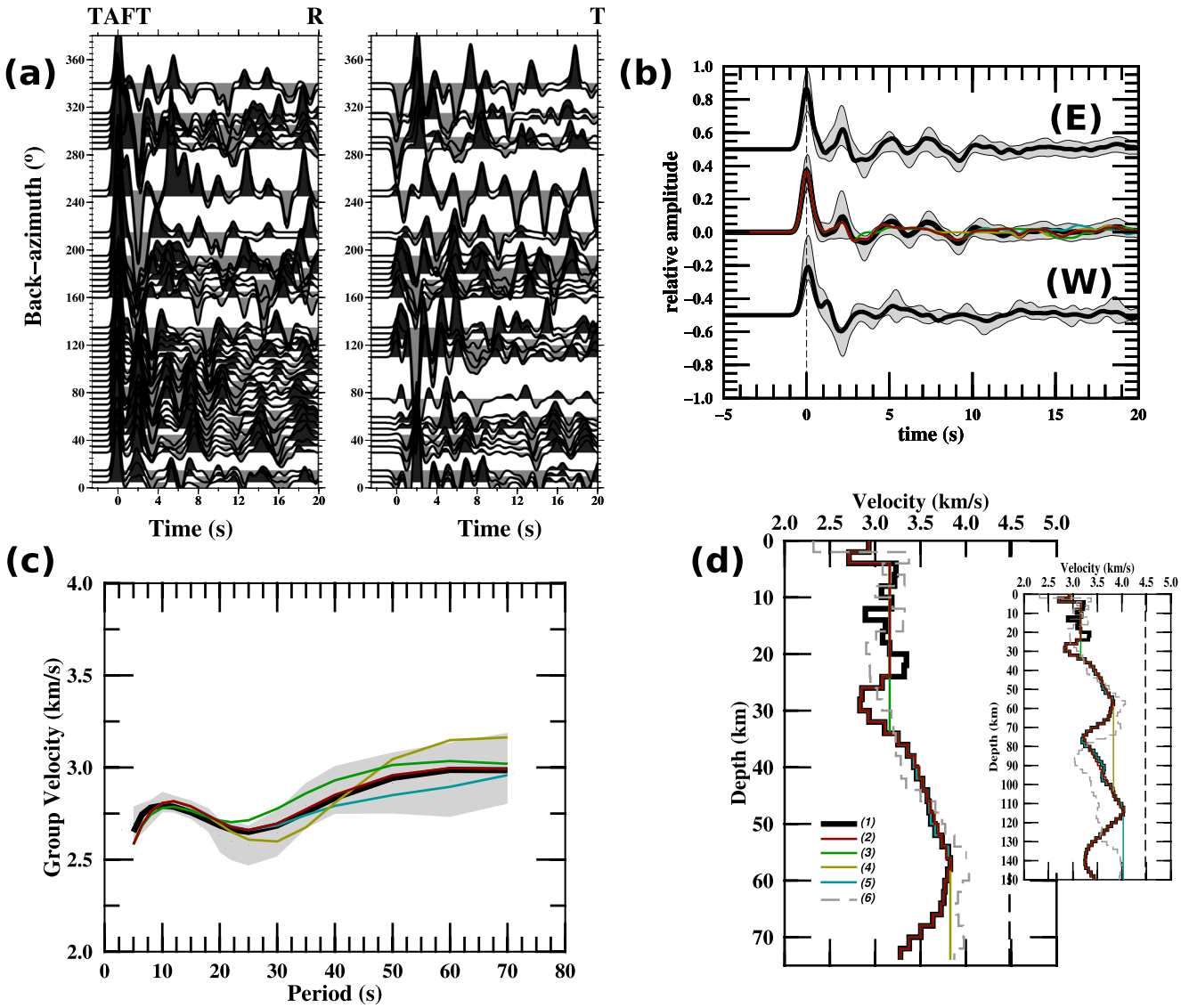

Figure 5. Summary of the TAFT (Figure 1) teleseismic receiver functions and surface wave data and analysis. The figure format is the same as in Figure 3. In (d), V_s(z) models for the crust and uppermost mantle beneath TAFT: (1) model derived from inverting the mean receiver function and pseudo-dispersion data; (2) simplified model; (3) effect of removing the LVZ centered at ~28 km depth; (4) effect of removing the LVZ centered at ~76 km depth; (5) effect of removing the LVZ centered below ~110 km depth; and (6) model derived from the inversion of the western receiver function stack and pseudo-dispersion data. The long-dashed black line is the inversion starting model.

arrival at ~13 s. The first motion of the transverse receiver function changes from negative to positive at a backazimuth of ~170° and back to negative at a backazimuth of ~350°. The CHBR stacked, 2.5 Gaussian receiver function (Figure 2b) contains a pronounced peak at ~4 s, a minor peak at ~2 s and a broad peak at ~13 s. The higher frequency 5.0 Gaussian receiver function shows that the broad ~13 s peak in the 2.5 Gaussian receiver function is composed of two closely-spaced but distinct peaks. The CHBR fundamental mode Rayleigh group velocity curve shows low wavespeeds at periods less than ~20 s with an Airy phase at ~18 s, a sharp rise in wavespeeds between 20–45 s period, and high wavespeeds (>3.5 km s^{-1}) at periods greater than ~50 s.

The inversion result for the CHBR receiver function and dispersion (Figure 2d) shows the average V_s model for this site has a very thin (~2 km, ~2.1 km s^{-1}) surface layer, a ~10 km-thick shallow crustal layer with V_s ~2.9 km s^{-1}, below which there is a ~10 km thick, ~3.1 km s^{-1} layer. Beginning at ~22 km depth, there exists a strong gradient (~0.10 s^{-1}) extending to ~32 km depth where the wavespeed is ~4.25 km s^{-1}. Beneath ~38 km depth, there is a low velocity zone (LVZ) extending to ~70 km depth. However, forward testing indicates that this

LVZ is not required by the receiver function and is only weakly constrained by the surface wave dispersion. Forward modeling tests also show that the double peak at ~13 s consists of two peaks, one from a positive velocity increase starting at ~100 km depth, and a second one which is a crustal reverberation. Thus, below ~36 km, V_s is nearly constant to ~100 km depth below which there is a second strong positive V_s gradient.

4.2. Jazmurian Depression

A significant change in the nature of the receiver functions and surface wave dispersion occurs near the latitude of the Jazmurian Depression, the sedimentary basin north of the Makran Range (e.g., Burg, 2018; Shahabpour, 2010). The basin, which may have only begun subsiding in the Late Pliocene (McCall & Kidd, 1982), has been the site of shallow marine sedimentation and volcanism, but the thickness of the basin has remained a question (Burg, 2018). The contact between the Jazmurian Depression and the Makran accretionary wedge has steeply-dipping normal faults related to the ongoing subsidence (Dolati & Burg, 2013).

Recordings from AJNT (Figures 1 and 3), which is located at the eastern edge of the Jazmurian Depression, are representative of the data from sites across this region. The receiver functions are complicated because they vary with azimuth, suggesting considerable structural complexity. The radial receiver functions have a positive arrival at ~2 s over the 30–270° backazimuth range and a strong negative arrival at ~5–6 s delay in the ~260–50° backazimuth range. The first arrival on the tangential receiver function is primarily negative for eastern backazimuth and primarily positive for northwestern backazimuths but, because of gaps in the recordings, it is not possible to constrain the azimuth where the change in polarity takes place. There is a prominent coherent positive tangential arrival at 5–6 s spanning the ~40–125° backazimuth range and a strong negative conversion at ~5 s in the 215–270° backazimuth range. The mean AJNT receiver function (Figure 3b) has a positive arrival at ~2 s, broad bounds between ~3.5–6.5 s that reflect the variability of the radial receiver functions at these delay times, and a negative arrival at ~8 s. Figure 3b shows stacked receiver functions computed from events with east and northwest backazimuths. Because a majority of the events recorded at AJNT are from eastern backazimuths, the mean and eastern receiver function stacks are similar. The northwestern receiver function stack, which consists of a smaller number (11) of individual receiver functions, differs from the mean receiver function with a secondary arrival interfering with the direct arrival, a positive arrival at ~3 s, and a strong, negative arrival at ~6 s. The AJNT short period (<20 s period) group velocity is somewhat higher (~2.7 km s^{-1}) than that observed in this period range at CHBR (~2.50 km s^{-1}), but the long period dispersion (>40 s) is slower (~3.25 km s^{-1}) than that which is observed in this period range at CHBR (~3.45–3.50 km s^{-1}).

AJNT has a complicated inversion $V_s(z)$ model with multiple LVZs. Teleseismic arrivals from the east partially sample the crust of the Sistan Suture Zone whereas arrivals from the northwest sample the crust of the Jazmurian Depression. Inversion of the mean AJNT receiver function results in a crustal model consisting of a low V_s (~2.6 km s^{-1}) surface layer, a ~22 km-thick layer with a 0.015 s^{-1} gradient where V_s increases from ~3.0–3.3 km s^{-1} at ~28 km depth, and a ~14 km thick layer with a 0.05 s^{-1} gradient where V_s increases from ~3.3–4.0 km s^{-1} at 42 km depth. Below this, there is a weak LVZ which forward modeling shows is not a robust feature of the model. Beneath this, V_s increases to ~4.1 km s^{-1} before again decreasing to below 4.0 km s^{-1}. Forward modeling shows that this decrease is also not a robust feature of the $V_s(z)$ model. V_s then increases to ~4.5 km s^{-1} at ~82 km depth but then decreases to less than ~3.8 km s^{-1} at ~105 km depth. This thick, deep LVZ is not constrained by the receiver function but is required by the dispersion data. The V_s (z) model derived from the northwestern stack is similar to the model derived from the mean receiver function to a depth of ~30 km, but between 40 and 50 km depth there is a significant LVZ with V_s dropping to ~3.2 km s^{-1}. This feature is the source of the strong negative arrival at ~6 s. Between ~50 and 65 km depth there is a 0.08 s^{-1} gradient with a $V_s > 4.5$ km s^{-1} at 65 km depth. Below this V_s drops to ~3.7 km s^{-1} and remains low to at least 150 km depth.

4.3. Sistan Suture Zone, Iranian Plateau

North of the Jazmurian Depression, the profile crosses the Sistan Suture Zone and the volcanic arc. The Sistan Suture is an abandoned, deformed accretionary prism (Bröcker et al., 2013; Tirrul et al., 1983) extending northward from the central Makran for ~700 km along the Iran-Afghanistan border. This feature formed when a branch of the Neo-Tethys Ocean closed between ~65 and 90 Ma, uniting the continental Lut and Helmand Blocks.

Continued convergence between these blocks has resulted in widespread folding and conjugate strike-slip faulting (e.g., Berberian et al., 1999; Camp & Griffis, 1982).

The data from ZHSF (Figures 1 and 4) are representative of the recordings from stations located on the Sistan Suture Zone away from the volcanic arc. There is a positive arrival at ~5 s spanning the entire backazimuth range, a significant negative arrival ~7.5–8 s spanning most of the ~25–130° backazimuth range and a second significant negative arrival at ~335–125° at ~2 s. The tangential receiver function is smaller in amplitude compared to the tangential receiver function observed at sites to the south. The tangential component first arrival is negative in the ~75–215° backazimuth range and positive in the ~220–50° backazimuth range. The stacked ZHSF receiver function (Figure 4b) is relatively simple with a prominent positive arrival at ~5 s, a significant negative arrival at ~2 s, a minor negative arrival at ~8 s, and minor positive arrivals at ~9.5 and 17 s. The fundamental mode Rayleigh group velocity curve is remarkably flat with short-period (<25 s) group wavespeeds of 2.9–3.0 km s^{-1} and long-period (>30 s) group wavespeeds of ~3.25 km s^{-1}.

The ZHSF inversion model is simple compared to the V_s models for the more southern sites. The shallow portion of the ZHSF model consists of a thin, ~2.85 km s^{-1} surface layer, a ~8 km thick ~3.25 km s^{-1} layer, a ~28 km thick ~3.4 km s^{-1} layer, a strong gradient (0.14 s^{-1}) between 38 and 42 km, a weak gradient (~0.01 s^{-1}) between 42 and 64 km depth, and a deep V_s (<3.65 km s^{-1}) LVZ. The sensitivity test shows that the upper mantle LVZ is weakly constrained by the ZHSF receiver functions but is required to fit the ZHSF surface wave dispersion.

4.4. Makran Volcanic Arc

TAFT is located on the slopes of the ~4,000 m high andesite strato-volcano Taftan (Figure 1) which is built on the ~2 km-high Sistan Suture Zone of the Iranian Plateau. Taftan consists of two main summits, Narkuh and Matherkuh. Narkuh is highly eroded while Matherkuh is partly covered by fresh-appearing, thick andesite lava flows. The Taftan edifice is primarily built of lava flows, but ignimbrites and pyroclastic flows also occur (Biabangard & Moradian, 2008). Zircon U-Pb data yield a cluster of ages at ~3.2 Ma but with some samples giving dates as young as 0.8 Ma (Pang et al., 2014), whereas $^{40}Ar/^{39}Ar$ dates range from ~7 to 0.7 Ma (Biabangard & Moradian, 2008). There are no credible reports of historical eruptions, although there is some speculation of minor activity in 1902 (Global Volcanism Program, 2020). The geochemical signatures of the Taftan magmas suggest that they were derived from the lithospheric-enriched melts by subduction metasomatic processes (Biabangard & Moradian, 2008). Saadat and Stern (2011) propose that, based on Sr and Nd isotropic ratios, the magmas that erupted at the Makran volcanic arc have no significant crustal contamination, implying a relatively thin (<40 km-thick) crust. They postulate that enrichment of large ion-lithophile elements, relative to light rare-earth-elements and depletion in Nb relative to large ion-lithophile elements are similar to most other convergent plate boundary arc basalts, suggesting that Makran basalts are formed by the melting of subcontinental mantle modified by dehydration of subducted Arabian Sea Plate. Furthermore, Saadat and Stern (2011) find that the Pb isotropic ratios of the basalts are consistent with a contamination of subducted sediments.

There is a coherent positive arrival at ~2 s in the radial receiver function in the ~10–120° backazimuth range followed by a coherent negative arrival at ~3.5 s and a significant negative arrival at ~2 s between ~170–190° which possibly extends to ~340° backazimuth. The first arrival of the tangential receiver function is positive in the ~100–190° range and negative across the ~300–75° backazimuth range. There is a strong, negative arrival at ~2 s for southeastern backazimuths. The mean and eastern backazimuth receiver functions have a prominent positive arrival at ~2 s and a minor positive arrivals at ~5 and 7 s. The western backazimuth receiver function has a strong negative arrival at ~2 s and a minor positive arrival at ~5 s. The TAFT group velocity curve is very flat with the mean group wavespeed never exceeding ~3 km s^{-1}.

The V_s structure derived from inverting the TAFT mean receiver function and the surface wave group velocity (Figures 5b–5d) is unusual in that at no point shallower than 150 km depth does V_s exceed ~4.1 km s^{-1}. The inversion model consists of a ~4 km-thick surface layer with V_s less than 3 km s^{-1}, a ~20 km-thick, ~3.2 km s^{-1} layer, a small LVZ centered at ~28 km depth, below which there is a positive gradient (0.050 s^{-1}) to ~58 km depth where V_s reaches ~3.85 km s^{-1}. Below this, there is a second negative gradient with V_s dropping to ~3.25 km s^{-1} at ~78 km depth. This structure overlies a third LVZ with V_s dropping to ~3.25 km s^{-1} at ~140 km depth. Sensitivity tests show that the shallower of the two deep LVZs is only weakly constrained by the surface wave dispersion and the deep LVZ is not constrained by the data. Inversion of the western backazimuth receiver function

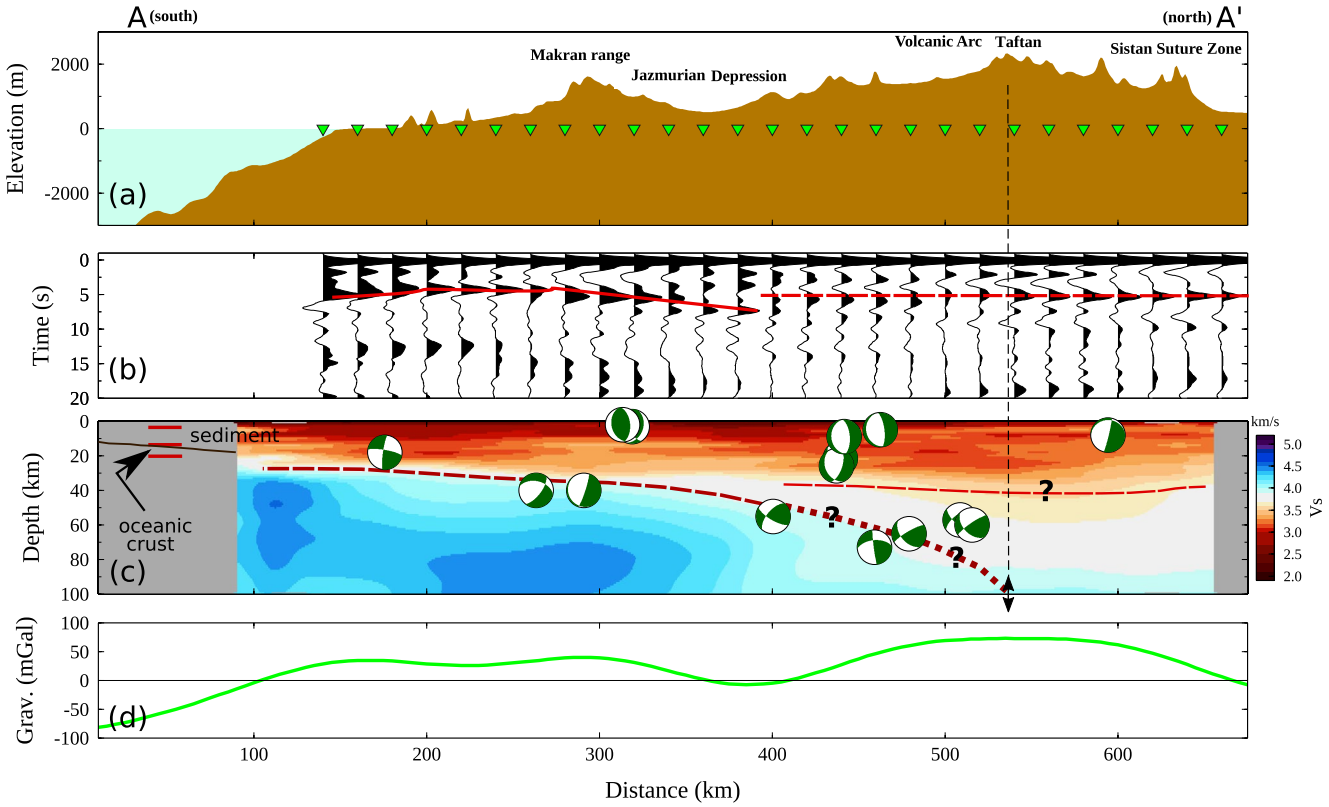

Figure 6. Variation in the nature of the radial receiver functions and the crust and uppermost mantle V_s structure along the Makran profile marked AA' in Figure 1. (a) The average topography (averaged ±50 km) along the profile with interpolated station locations (green inverted triangles) plotted at sea level. (b) The variation in the nature of the interpolated radial receiver functions along the profile. The solid red line at the south end of the profile indicates the arrival which we interpret to be the interfering conversions from the top of the oceanic basement and the oceanic Moho, and the dashed red line at the northern end of the profile indicates the arrival we interpret to be the conversion of the continental Moho beneath south-central Iran. (c) The variation of the V_s structure along the profile. Off the coast at the southern end of the profile, the solid black line indicates the approximate position of the oceanic basement interface detected in marine experiments located somewhat to the southeast of profile AA' (Kopp et al., 2000); the three red lines denote the top of the sedimentary layer, the top of the oceanic basement and oceanic Moho found in the controlled-source experiment located somewhat to the southwest of the profile (Niazi et al., 1980). The short-dashed red line beneath the southern portion of the receiver function profile indicates our interpretation of the oceanic Moho with the dotted line where the Moho is less clear. The long-dashed red line starting at ~400 km indicates a possible Moho beneath the volcanic arc and Sistan Suture Zone. Over-plotted on (c) are the earthquake mechanisms ±200 km from the profile taken from Penney et al. (2017). The focal spheres have been rotated by 90° and displayed from the side to correspond to the cross-section view of the wavespeed structure. A wavespeed scale for the V_s structure is shown at the left in (c). (d) The variation of GOCE free-air gravity along the profile. All distances refer to the southern end of the plot.

results in a structure above ~55 km depth, which is similar to that of the inversion result of the mean receiver function but reaching a slightly higher V_s of ~4.0 km s^{-1} at ~58 km depth. Below this, V_s remains approximately constant to ~72 km depth but beneath this, there is an extensive LVZ extending to at least 130 km depth.

4.5. Interpolated Receiver Function Profile

In the previous subsections, we discussed inversion results for seismic data recorded at sites located on four representative tectonic structures across the Makran Subduction Zone of southern Iran. The inversion results for the remaining recording sites are summarized in Table 1. To equalize the lateral sampling of the receiver functions and surface wave dispersion, we have interpolated the receiver functions as described in Section 3.2, and the interpolated wavefield and its inversion model are shown in Figure 6. As pointed out by Chai et al. (2015), interpolation of the receiver function wavefield accentuates the first-order features in the receiver function response and suppresses the large-amplitude fluctuations at individual stations that complicate receiver function analysis. In addition, the interpolation of the receiver function wavefield compensates for the difference in spatial sampling of receiver functions and surface waves when the two data are jointly inverted.

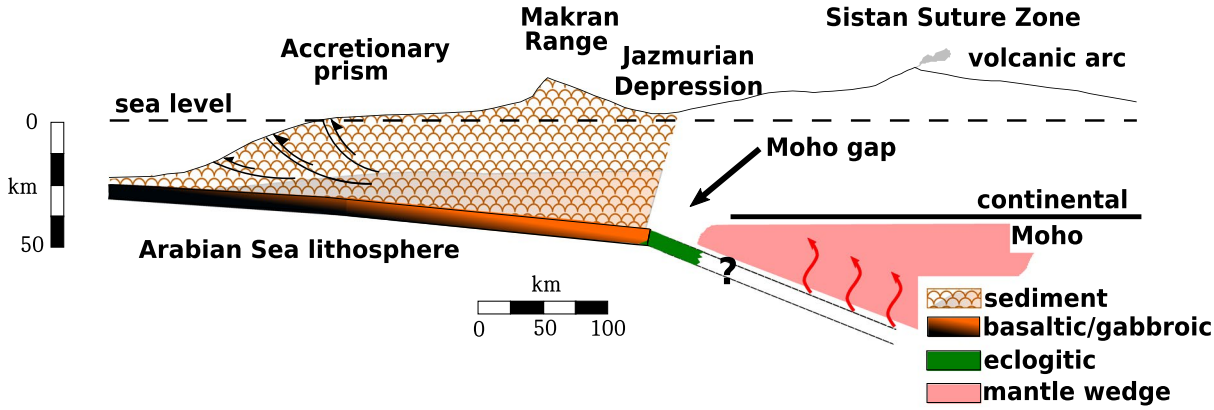

Figure 7. Summary schematic of the structure for the western Makran Subduction Zone derived in this study. The incoming Arabian Sea Plate begins subducting at a very shallow angle beneath the accretionary complex. Sediments as thick as 25 km accumulate over the incoming plate (brown scalloped), and the trench/forearc is clogged with sediment. Stresses due to the thickening sediment and tectonic compression cause shortening and uplift (e.g., Berberian & King, 1981; Haghipour & Burg, 2014; Jackson & MKenzie, 1984; Penney et al., 2017; Page et al., 1979; Snead, 2002) of the sediments that form the coastal plane and the Makran Range. As the oceanic crust is buried deeper beneath the sediment, the shear wavespeed of the basaltic/gabbroic crust (black to brown transition) likely alters to blueschist metamorphism. When the oceanic crust reaches a depth of ~50 km, the basaltic/gabbroic crust begins to transform to eclogite (green) and the increased density causes this portion of the plate to become gravitationally unstable and the angle of subduction becomes steeper. This takes place in the vicinity of the Jazmurian Depression. The entrained sediments and the metamorphic reactions transforming the basaltic/gabbroic oceanic crust to eclogite release large volumes of H_2O-rich fluids (red arrows) into the overlying mantle wedge (pink). The rising fluids lead to the serpentinization of the mantle wedge peridotite, lowering the density and velocity. An effect of the metamorphic reaction taking place in the oceanic crust and the overlying mantle wedge is to render the Moho invisible in the receiver functions from the nose of the mantle wedge (Moho gap). Farther north, the seismic profile crosses the continental crust of the Sistan Suture Zone and the volcanic arc. The crust is ~40 km thick beneath the Sistan Suture Zone, similar to the crustal thickness beneath central Iran (Ahmadzadeh-Irandoust et al., 2022) and there is no discernible continental root beneath the elevated region of the volcanic arc.

Figure 6b shows a smooth variation in a strong, positive arrival at ~5 s delay near the coast, to ~4 s delay immediately south of the Makran Range. This arrival disappears at ~7 s delay at ~375 km distance along the profile beneath the eastern Jazmurian Depression. There is a second positive arrival at ~2 s delay which has significant amplitude at the coast but then decreases in amplitude and disappears ~100 km north of the coast. North of ~410 km, there is a low amplitude positive arrival at a delay time of ~5 s which increases in amplitude north of ~425 km. Beneath the region of the volcanic arc, there is a strong positive phase at ~2 s immediately followed by a strong negative arrival at ~3.5 s with another significant negative phase at 7–8 s delay which has its peak amplitude beneath the volcanic arc.

Figure 6c displays the variation in the V_s structure beneath the profile derived from the inversions of the interpolated receiver functions and surface wave dispersion. The shallow structure is composed of material with $V_s <$ 3.5 km s^{-1} across the whole profile. In the southern portion of the profile there is a thin band of material with a wavespeed of 3.6–3.9 km s^{-1} at a depth ~25–30 km which broadens to the north of ~350 km. North of ~425 km the very slow wavespeed, near-surface material thins and approaches zero thickness at the northern end of the profile. However, very slow wavespeed (~3.6 km s^{-1}) occurs from ~40 km depth and $V_s < 4.1$ km s^{-1} wavespeed material persists to at least 100 km depth beneath the volcanic arc.

5. Discussion

We have derived a shear wave velocity model that extends to a ~100 km depth beneath a ~400 km-long profile of seismographs oriented approximately parallel to the convergence vector and stretching from the Makran coast to a point ~400 km north on the southern Iranian Plateau (Figure 1). The model was obtained by jointly inverting receiver functions from seismic data recorded at 26 sites along the profile with fundamental mode Rayleigh group velocity dispersion determined from ambient noise and regional earthquake analysis. Figure 7 summarizes the Makran structure we discussed in Section 4. This model confirms the conjectures of the large-scale features proposed in early papers on the region (e.g., Farhoudi & Karig, 1977; Jackson & MKenzie, 1984).

5.1. Coastal Sedimentary Structure

The high sedimentation rate and shallow angle of the incoming plate has led to the formation of an accretionary prism (Figure 1) ~350 km wide, of which only the frontal 100–150 km is currently submarine. During the initial period of the Arabian Sea Plate subduction, the accretionary wedge grew by accreting Himalayan turbidites deposited in the paleo-Indus deep-sea fan (Grando & McClay, 2007; Kukowski et al., 2001). The uplift of the Murray Ridge System during the Early Miocene (Gaedicke et al., 2002) shifted the Indus sediments to the south and, since that time, the Makran accretionary complex has been maintained largely by the recycling of sediments coming from the erosion of the older prism and conveyed to the front of the modern accretionary complex through a series of river and canyon systems (Haghipour & Burg, 2014; Haghipour et al., 2015), and by incorporating abyssal sediments scraped off the subducting Arabian Sea Plate (Burg, 2018; Grando & McClay, 2007; Platt et al., 1985). The present-day Himalaya-derived sediments contribute little to the Makran accretionary wedge (Ellouz-Zimmermann, Lallemant, et al., 2007). Mud volcanoes are prevalent along the Makran coastal region (Negaresh, 2008; Wiedicke et al., 2001), suggesting over-pressured sediments at deeper depths in the accretionary wedge. Tectonic compression and stresses due to the thickening sediment cause shortening and deformation of the sediments as seen in off-shore folding and faulting (e.g., Grando & McClay, 2007; Kopp et al., 2000), the uplifted coastal marine terraces (e.g., Page et al., 1979; Snead, 2002), the on-shore folding (e.g., Farhoudi & Karig, 1977), thrust faulting (e.g., Berberian & King, 1981), uplift (e.g., Haghipour & Burg, 2014) of the Makran Range, and the high angle (40–50°) reverse-faulting mechanisms for shallow earthquakes (e.g., Jackson & MKenzie, 1984; Penney et al., 2017).

Modeling of receiver function and surface wave data from coastal sites shows the presence of a ~22–28 km-thick low wavespeed sedimentary cover. Near the coast, the sedimentary section V_s increases from ~2.5 km s^{-1} at the surface to ~3.7 km s^{-1} at ~22 km depth. The on-shore sedimentary structure of our model is consistent with the off-shore structures determined from controlled-source seismic recordings (e.g., Fruehn et al., 1997; Grando & McClay, 2007; Kopp et al., 2000; Niazi et al., 1980; ; Smith et al., 2012). Similar thick sedimentary structures are observed in other present-day accretionary structures and in accretionary structures in the geologic record (Cawood et al., 2009).

The sparse wide-angle recordings of Niazi et al. (1980) (Figures 1 and 6c) ~200 km southwest of our profile, found the oceanic crust to be ~20 km-thick and consisting of a 13–14 km-thick low wavespeed (V_p ~4 km s^{-1}) layer over a 6–7 km thick oceanic crust. Near-vertical controlled-source seismic recordings (Grando & McClay, 2007) along several profiles ~100 km southwest of our seismic profile found that at the deformation front, abyssal sediments are being scraped from the underthrusting Arabian Sea Plate, forming an imbricate fan of active thrust faults. Further north, they found that a previously deposited 4 km-thick Himalayan turbidite sequence is underplating and uplifting the wedge and the mud volcanoes are spatially related to the onset of the underplating of sediments (Grando & McClay, 2007). Kopp et al. (2000) found, from active-source data collected off the Pakistan coast ~200 km east of our profile, that the upper part of the accretionary prism consists of ~10 km of unconsolidated sediments overlying a thick layer of more consolidated underplated sediment (Figure 6c). They determined that the shallow sediment layer is characterized by a low velocity gradient (~0.16 s^{-1}). From their wide-angle measurement, Kopp et al. (2000) conclude that the décollement steps down toward the north, thus allowing for substantial underplating, and they suggest that ~3 km of the incoming sedimentary section is thrust beneath the deformation front. Mass balanced calculations suggest that ~50% of the down-going sediments are incorporated into the wedge by subcretion (Platt et al., 1985, 1988). The projection of the off-shore structure derived from the controlled-source seismic experiments (e.g., Ellouz-Zimmermann, Lallemant, et al., 2007; Fowler et al., 1985; Fruehn et al., 1997; Kopp et al., 2000; Smith et al., 2012) is consistent with the on-shore structure we find in our study (Figure 6c).

Haberland et al. (2021) determined a compressional velocity model for the on-shore accretionary wedge structure from active seismic source recordings along three ~200 km-long lines perpendicular to the coast. Their easternmost profile is coincident with the receiver function profile in this study. Figure 8 compares the average V_p from the active seismic experiment with the average V_s from the receiver function/surface wave analysis at two points, one at the coast and a second ~50 km north of the coast (Figure 1). The V_p averages at the two points are formed from the tomographic model for the easternmost seismic profile of Haberland et al. (2021). The average V_p structure near the coast (point a, Figure 1) consists of a strong, ~2–3 km thick near-surface gradient zone where V_p increases from ~3.2–5 km s^{-1}, overlying a ~10 km-thick, V_p ~5 km s^{-1} upper crustal layer, below which there

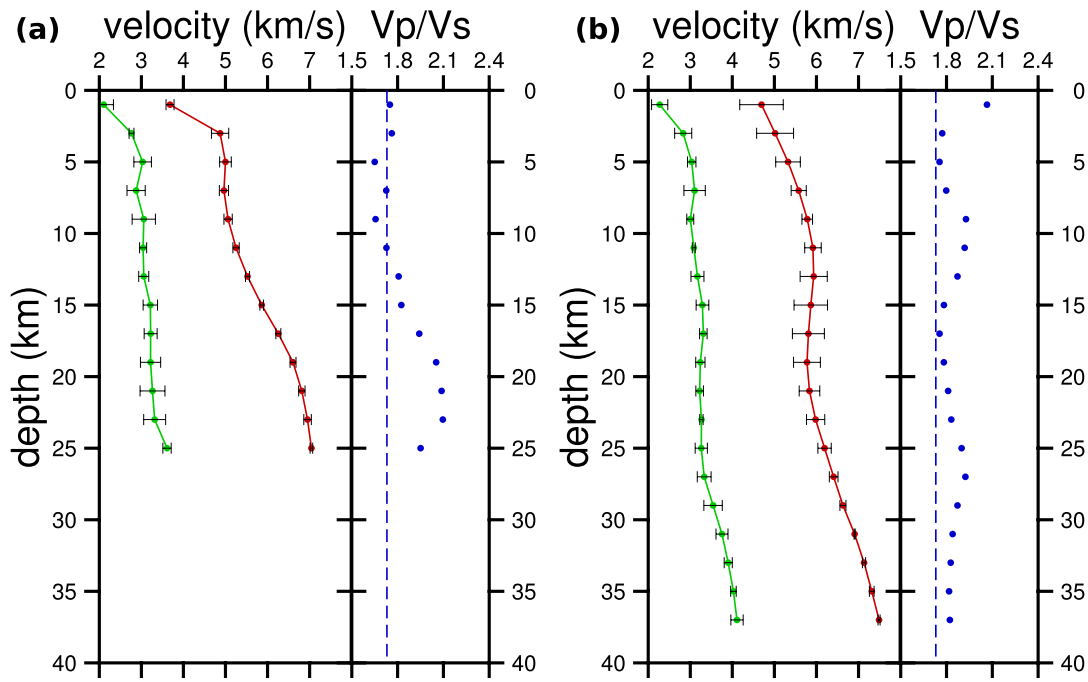

Figure 8. Shallow V_p (red dots with error bars), V_s (green dots with error bars) and V_p/V_s (blue dots) at two locations where active-source and passive-source-derived structure exist (see Figure 1 for locations). The V_p and V_s shown are the mean and standard deviation in a 10 km radius region about the points a and b (Figure 1). The thin blue dashed line is positioned at 1.73. The *x*-axes units are wavespeed in km s^{-1} for V_p and V_s or wavespeed ratio for V_p/V_s.

is positive gradient where V_p increases to ~7 km s^{-1} at ~22 km depth (Figure 8a). Haberland et al. (2021) do not see the basement near the coast. Further inland (point b, Figure 1), the average V_p structure consists of a 12 km thick gradational section with V_p increasing from ~4.5 km s^{-1} at the surface to ~5.9 km s^{-1}. Below this, there is a ~10 km thick section with a near uniform V_p of ~5.9 km s^{-1} above a positive gradient (0.10 s^{-1}) extending to the base of their model (Figure 8b). Between 60–90 km inland from the coast, there is a band of reflecting elements at 30–35 km depth dipping northward at ~8° ± 2° which Haberland et al. (2021) associate with the base of the subducting oceanic crust. Also included in Figure 8 are V_p/V_s profiles for the two points. In the upper ~15 km near the coast the V_p/V_s -ratio is close to 1.73 but deviates below ~15 km depth with V_p/V_s reaching ~2.1 at ~23 km depth. This high V_p/V_s layer could indicate over-pressure in the subducting sediments and the source of the mud volcanoes near the coast. At the point ~50 km from the coast the V_p/V_s is close to 1.73 at all depths.

5.2. The Subducting Arabian Sea Plate

Beneath the sedimentary cover near the coast at depths greater than ~23 km, there is a 6–8 km-thick strong gradient layer in which V_s increases from ~3.5–4.2 km s^{-1}. This feature is compatible with the receiver function signature expected from layers 2 and 3 of the oceanic crust. The base of the gradient has a shallow 4 ± 2° northward dip (Figure 6c). This is consistent in depth and dip with the band of reflectors observed in the controlled-source seismic data (Haberland et al., 2021). The receiver function arrival at 5–6 s is a composite of energy from several conversions, but is primarily from the oceanic Moho (Figure 2b). This phase disappears ~250 km north of the coast at the northern fringe of the Jazmurian Depression at a delay time corresponding to a depth of ~50 km (Figure 6b). Between the coast and the Jazmurian Depression where seismology shows the flat slab, the free-air gravity anomaly is 25 ± 5 mgals (Figure 6d).

The only information on the structure of the basaltic/gabbroic oceanic crust off the western Makran is the low-resolution model from the short-duration OBS recording of Niazi et al. (1980) who found a 6–7 km-thick, V_p ~6.7 km s^{-1} layer below the sediments which they hypothesized was the oceanic crust. This V_p wavespeed and oceanic crustal thickness is consistent with the V_s wavespeed and thickness observed near the coast in our model. In a more detailed active-source seismic study conducted off the eastern Makran coast, Kopp et al. (2000) found

an oceanic crust ~9 km thick dipping about 3° northward and consisting of a shallow low velocity gradient and a strong velocity contrast (V_p 5.7–7.0 km s^{-1}) between oceanic layers 2 and 3.

Figure 6b shows a decrease in the Ps delay time of approximately a second at ~220 km distance beneath the near-coastal sites, suggesting a significant shallowing of the Moho. This is not a prominent feature in the inverted velocity model (Figure 6c). Haberland et al. (2021) found a similar uplift in the Moho structure from their controlled-source recordings along a refraction profile that coincides approximately with our receiver function profile. Unpublished work (Irandoust, 2021; Mokhtarzadeh, 2022) indicates that this feature extends east-west along the coast almost perpendicular to the profile. The position of this apparent uplift is approximately where one might expect the outer rise uplift (Melosh & Raefsky, 1980), but the amplitude is much too great for this to be an outer rise structure similar to that observed in other subduction zones. The amplitude of this uplift decays to the west, but it has a similar amplitude eastward into Pakistan (Irandoust, 2021). The receiver function profile location coincides approximately with the boundary between the western and eastern Makran. Subduction in eastern Makran is hindered by the stable block to its north, whereas subduction in the west has less opposition from the overriding plate. It may possibly be that this change in subduction has caused the uplift of the Moho.

Motaghi et al. (2020); Penney et al. (2017) and Taghizadeh-Farahmand et al. (2015) have published results for the CHBR (Figure 1) receiver function. Taghizadeh-Farahmand et al. (2015) recognize a converting interface 33 ± 2 km below CHBR which they identified as the Moho and concluded from this that there was no crustal thickening beneath CHBR nor evidence of collisional processes taking place in this region. Penney et al. (2017) surmised that the strong gradient at 26 ± 2 km depth in their CHBR receiver function inversion model was the top of the oceanic basement; they found a similar crustal structure to the east beneath the Makran of Pakistan (TURB, Figure 1). Motaghi et al. (2020) used HK-stacking of receiver functions from recordings from CHBR and the nearby station NGCH and arrived at a similar conclusion to that of Penney et al. (2017). Motaghi et al concluded that the double peak at ~13 s in the receiver functions consisted of the arrival of reverberations from the top and bottom of a 4.5 km- and 7 km-thick hidden-layer oceanic crust beneath NGCH and CHBR, respectively. However, their conclusion implies that the oceanic crust would have an anomalously low V_p/V_s. Our sensitivity test (Figure 2) shows that this double peak at ~13 s in the CHBR receiver functions does arise from interfering arrivals, one being the crustal multiple and the second a conversion from a V_s increase at ~100 km depth.

The nature of the Moho conversion below the receiver function profile is similar to the Moho pattern observed beneath Cascadia (e.g., Audet et al., 2009; Bostock et al., 2002; Nicholson et al., 2005). In the south across the Makran accretionary prism, there is a strong Moho conversion. Below the Jazmurian Depression the Moho conversion in the receiver functions becomes weak and disappears (Figure 6b) at a delay time corresponding to a depth of ~50 km at a distance about ~250 km north of the coast. This implies a weak or non-existent velocity contrast which probably signifies the transformation of the basaltic/gabbroic oceanic crust to eclogite. V_s for basalt and eclogite at this depth are ~4.0 km s^{-1} and ~4.7 km s^{-1} respectively, compared to peridotite ~4.6 km s^{-1} (Christensen, 1996; Christensen & Mooney, 1995), rendering the oceanic Moho nearly invisible. The accompanying increase in density, possibly by as much as 15% (e.g., Brocher, 2005) would cause the incoming Arabian Sea Plate to become gravitationally unstable and descend more steeply into the mantle. However, it cannot be ruled out that the disappearance of the oceanic Moho arrival is due to a sudden steepening in the dip of the subducting Arabian Sea Plate.

Our profile recording allows us to track the subducting oceanic lithosphere from beneath the accretionary prism to ~50 km depth. Earthquake mechanisms with well-constrained hypocentral depths (e.g., Penney et al., 2017) (Figure 6c) allow the subducting oceanic plate to be traced to somewhat deeper depths. Near the coast, there are several shallow thrust-faulting events. Farther north, there is a group of normal-faulting earthquakes at depths ~50 km (at 400–500 km on Figure 6c) in the vicinity of where the Moho arrival disappears. The M_w 7.7 Khash earthquake (Barnhart et al., 2014) resulted from normal faulting at ~75–80 km deep somewhat to the east of the receiver function profile. Penney et al. (2017) pointed out that the normal-faulting earthquakes have an ~ENE–WSW linear distribution in map view parallel to the strikes of their nodal-planes and are observed across the longitudinal extent of the subduction zone. Penney et al. (2015) took the fault planes of the shallow thrust earthquakes (Figure 6c) to be the northward-dipping nodal planes and then, if these events occur on the subduction interface, the dips of 8–10 ± 5° of their nodal planes provide an estimate of the dip of that interface near the coastline. This is close to, but somewhat steeper than, the dip of the subducting interface inferred from the receiver-function/surface-wave and active-source models. Penney et al. (2017) further suggested that the dip of the

seismogenic zone inferred from the earthquake distribution appears to steepen to the north of the normal-faulting earthquakes and proposed that the normal-faulting events probably represent extension at a hinge in the subducting Arabian Sea Plate.

One of the normal-faulting earthquakes occurred almost directly beneath the Bazman volcano at a depth of 74 km (Jacob & Quittmeyer, 1979). This implies that the subduction interface is no deeper than ~90 km under this part of the volcanic arc, allowing for a ±15 km possible error in the earthquake depth. The location of the volcanic arc is affected by various factors besides the depth of the slab, but globally, the depth of the subducting slab has been found to be in the 100–120 km depth range below the volcanic arc (Syracuse & Abers, 2006). Global body-wave tomographic studies (e.g., Van der Meer et al., 2018) show a steeply (~45°) northward-dipping high V_p-wavespeed structure in the upper mantle (~280–600 km depth) beneath central Iran. Models of the shallow upper mantle structure (e.g., Shad Manaman et al., 2011) show the presence of a northward-dipping high wavespeed structure. When projected back to a shallow depth, both features intersect approximately with the region where the receiver function signature of the oceanic plate disappears.

One feature of the oceanic slab structure is perplexing – the south-to-north V_s variation. High V_s wavespeeds in our model occur near the coast (100–125 km) and further inland (200–325 km) (Figure 6c), but there are zones with lower wavespeed (125–200 km and >325 km) (Figure 6c). This portion of the structure is primarily constrained by the surface wave dispersion and there can be a reduction in the amplitude of the deeper structure due to the decreased sensitivity of the surface waves with depth. However, the lateral variation in V_s along the profile suggests that this is not the cause since the sensitivity of the surface waves is very close to uniform along the profile. The observed variation may arise from faulting in the crust and uppermost mantle of the subducting oceanic lithosphere. Bending-related faulting in subduction zones has been recognized world-wide (e.g., Contreras-Reyes et al., 2011, 2015; Grevemeyer et al., 2007; Ivandic et al., 2008; Ranero & Sallarès, 2004) and these faults can provide pathways that allow water to infiltrate the crust and uppermost mantle, altering the basalt/gabbro of the oceanic crust and peridotite of the uppermost mantle and affecting the seismic wavespeeds. V_p and V_s in the uppermost mantle can decrease from 8.2 to 7.7 km s^{-1} and 4.7 to 4.2, respectively (e.g., Christensen, 1972, 2004; Grevemeyer et al., 2018). If this is the cause of the lower wavespeed of the subducting Arabian Sea Plate, it is puzzling as to why this would affect portions of the Plate differently.

5.3. Sistan Suture Zone, Volcanic Arc and Mantle Wedge

North of the Jazmurian Depression, the receiver function/surface wave inversion shows that the continental crust of the southern Iranian Plateau has an average V_s of 3.55 ± 0.05 km s^{-1}, an almost flat Moho at a depth of 40–45 km based on the nearly uniform Ps delay time (Fig. 6b), and a sub-Moho mantle V_s of 3.75 ± 0.05 km s^{-1} in the 50–80 km depth range. However, the location of the Moho beneath the volcanic arc is not clear in our model (Figure 5d). In our inversion model (Figure 6c), the Moho appears as a weak velocity increase. In a global subduction zone survey, Bostock (2013) suggested that the large volume change associated with the transformation of the basaltic/gabbroic oceanic crust to eclogite may rupture the plate boundary, allowing fluids to penetrate the forearc mantle wedge leading to the serpentinization and melting of the mantle wedge rocks. The serpentinization and the free fluids can diminish, erase or even invert the velocity contrast of the Moho of the overriding plate. Below the Sistan Suture Zone, there is a thin upper mantle lid below which is a substantial mantle LVZ where V_s drops to ~3.5 km s^{-1} at ~130 km depth. Sensitivity tests (Figures 4 and 5) show that the very low V_s in the uppermost mantle is required.

Our seismic profile cuts across the volcanic belt between the active volcanoes of Bazman and Taftan; one of our recording sites is on Taftan (Figure 1). There is a pronounced low velocity layer (LVL) in the crust seen in the receiver function as the significant negative arrival that starts at ~410 km along the profile and terminates at ~580 km (Figure 6b). This appears as a LVL in the lower crust in the inversion structures of the individual receiver functions (Figure 5).

In subduction zones, the crust of the incoming plate comes in contact with the crust of the overriding plate in the forearc region and then descends into the mantle. Wilson (1954) was the first to suggest that H_2O-rich fluids are generated from the Wadati-Benioff zones. In addition to the release of H_2O from the entrained sediments as the oceanic crust is carried to deeper depths in the mantle, the metamorphic reactions transforming the basalt/gabbroic oceanic crust to eclogite release large amounts of H_2O-rich fluids into the overlying mantle wedge (e.g.,

Christensen, 2004; Peacock, 1993, 1996). The rising fluids cause extensive hydrothermal alteration and lower the solidus of the material in the overlying mantle wedge, causing serpentinization and melting of the mantle peridotite. Serpentinization of the mantle wedge has now been documented in most subduction zones where detailed seismic studies have taken place (e.g., Eberhart-Phillips et al., 2005; Grevemeyer et al., 2018; Husen et al., 2003; Kamiya & Kobayashi, 2000; Kuwatani et al., 2011; Reynard, 2013; Seno et al., 2001; Sodoudi et al., 2006; Xia et al., 2008). Serpentinization causes a substantial lowering of the wavespeed and density of the mantle wedge (Peacock, 1996). One effect of the serpentinized peridotite is to reduce the seismic signature of the overlying continental Moho, and, in extreme instances, can result in an inverted Moho (Bostock et al., 2002). The conversion from the Arabian Sea Plate Moho is clear beneath the accretionary prism but deepens and disappears at ~400 km (Figure 6b). In this same region, earlier weak arrivals exist which are probably the first indication in the receiver functions of the conversion from the continental Moho. This disruption in the seismic signature of the Moho occurs in the Makran Subduction Zone forearc region where the dip of the subducting Arabian Sea Plate steepens. Bostock et al. (2002) proposes that the weak conversions from the continental Moho may result from serpentinization of the peridotite in the mantle wedge of the Cascadia Subduction Zone.

Antigorite, the high pressure/temperature form of serpentine, is stable over a wide range of pressure and temperature conditions (e.g., Ulmer & Trommsdorff, 1995; Wunder & Schreyer, 1997). In the mantle wedge between ~90 and 120 km depth where arc magmas are generated, antigorite is likely to be the main hydrous mineral (e.g., Hyndman & Peacock, 2003; Ji et al., 2013; Schmidt & Poli, 1998). Laboratory results (Ji et al., 2013) find that for 100% serpentinization to antigorite, V_p and V_s decrease to 6.68 km s^{-1} and 3.67 km s^{-1}, respectively, and that V_p/V_s increases to 1.81. Serpentinization substantially decreases the density. Unaltered peridotite has a density of ~3,200 kg m^{-3} whereas the density of 100% serpentinization peridotite is ~2,500 kg m^{-3} (e.g., Christensen, 1996; Hyndman & Peacock, 2003). However, the $V_p \approx 7.75$ km s^{-1} observed in the Makran mantle wedge (Al-Lazki et al., 2014) suggests that the degree of serpentinization is ~20%, in the range inferred for other subduction zones (e.g., Chou et al., 2009; Kamiya & Kobayashi, 2000; Ranero & Sallarès, 2004; Van Avendonk et al., 2011; Wada et al., 2008). Serpentinization of 15%–30% would reduce the density to ~3,000 kg m^{-3} (Hyndman & Peacock, 2003).

Between the continental Moho and the inferred depth of the Arabian Sea Plate, the V_p (Al-Lazki et al., 2014) and V_s (this study) are low and give a V_p/V_s of ~2.05, significantly higher than possible for 100% antigorite (Ji et al., 2013). The receiver functions indicate a nearly flat continental Moho across the region (Figure 6b), and there is no crustal root beneath the elevated region of the volcanic belt. The free-air gravity anomaly over the volcanic belt is ~75 mGal (Figure 6d) indicating partial compensation. However, the nearly flat Moho implies the partial compensation of the volcanic zone topography occurs from a low density sub-Moho mantle. The average elevation of the volcanic arc is ~1.75 km. Assuming a mean density of 2850 kg m^{-3} for the crust, the free-air gravity anomaly would be ~200 mGal. Therefore, partial compensation of the elevation must occur in the mantle. If this compensation occurs in a 60 km-thick layer between the base of the crust at ~40 km depth and the inferred depth of the subducting Arabian Sea Plate at ~100 beneath the volcanic arc, it implies a reduction in density of 50 kg m^{-3} to account for the observed gravity anomaly or an upper mantle density of 3,150 kg m^{-3}, similar to that inferred for other subduction zones (Hyndman & Peacock, 2003).

Although the mantle wedge V_s beneath the volcanic arc is consistent with 100% serpentinization of the peridotite to antigorite (Ji et al., 2013), this degree of serpentinization is incompatible with the observed free-air gravity anomaly over the volcanic belt and the inferred V_p/V_s of the mantle wedge from the V_p (Al-Lazki et al., 2014) and V_s found in this study. The high V_p/V_s ratio compared to that for 100% antigorite suggests that the low V_s we observe for the mantle wedge results from a fluid-rich or partially molten mantle wedge. Hammond and Humphreys (2000) find ~8% reduction for upper mantle V_s for realistic partial melt geometries per percent of partial melt. The V_s we observe in the mantle wedge beneath the volcanic arc therefore implies the presence of ~1%–2% partial melt. This is consistent with the findings of Saadat and Stern (2011) that Makran arc basalts formed as a result of a low degree of partial melting of the mantle wedge which is only moderately modified by subducted components.

6. Summary

We have derived a shear wave velocity model extending to ~100 km depth beneath a ~400 km-long profile of seismographs oriented approximately parallel to the convergence vector and stretching from the Makran coast to a point ~400 km north on the southern Iranian Plateau (Figure 1). The model was obtained by jointly inverting receiver functions and fundamental mode Rayleigh group velocity dispersion from seismic data recorded at 26 sites along the profile. Modeling of receiver function and surface wave data from coastal sites shows the presence of a ~22–28 km-thick low wavespeed sedimentary cover. Near the coast, the sedimentary section V_s increases from ~2.5 km s^{-1} at the surface to ~3.7 km s^{-1} at ~22 km depth. A comparison of the V_s structure of the accretionary prism sediment cover with the V_p results of Haberland et al. (2021) shows that in the upper ~15 km near the coast the V_p/V_s -ratio is close to 1.73 but deviates below ~15 km depth with V_p/V_s reaching ~2.1 at ~23 km depth. This high V_p/V_s layer could indicate over-pressure in the subducting sediments and the source of the mud volcanoes near the coast. At the point ~50 km from the coast the, V_p/V_s is close to 1.73 at all depths.

Beneath the sedimentary cover near the coast there is a 6–8 km-thick strong gradient layer in which V_s increases from ~3.5–4.2 km s^{-1}, a feature that is compatible with the receiver function signature expected from layers 2 and 3 of the oceanic crust. The base of the gradient has a shallow 4 ± 2° northward dip (Figure 6c), consistent in depth and dip with the band of reflectors observed in the controlled-source seismic data (Haberland et al., 2021). The nature of the oceanic Moho conversion below the Makran profile is similar to the oceanic Moho pattern observed beneath a number of other subduction zones (e.g., Fukao et al., 1983; Maekawa et al., 1993; Ohmi & Hurukawa, 1996; Peacock & Wang, 1999; Rondenay et al., 2008). In the south across the Makran accretionary prism, there is a strong Moho conversion. Below the Jazmurian Depression, the Moho conversion in the receiver functions becomes weak and disappears (Figure 6b) at a delay time corresponding to a depth of ~50 km. This implies a weak or non-existent velocity contrast which probably signifies the transformation of the basaltic/gabbroic oceanic crust to eclogite.

North of the Jazmurian Depression, the receiver function/surface wave inversion demonstrates that the continental crust of the southern Iranian Plateau has an average V_s of 3.55 ± 0.05 km s^{-1}, an almost flat Moho at a depth of 40–45 km, and a sub-Moho mantle V_s of 3.75 ± 0.05 km s^{-1} in the 50–80 km depth range. The conversion from the Arabian Sea Plate Moho is clear beneath the accretionary prism but deepens and disappears at ~400 km (Figure 6b). In this same region, the weak arrival at ~5 s in the receiver functions appears and grades to the north into the continental Moho arrival. This disruption in the seismic signature of the Moho occurs in the Makran Subduction Zone forearc region where the dip of the subducting Arabian Sea Plate steepens.

The fact that weak continental Moho conversions may result from serpentinization of the peridotite of the mantle wedge has been proposed for Cascadia (Audet et al., 2009; Bostock et al., 2002; Nicholson et al., 2005). The $V_p \approx 7.75$ km s^{-1} observed in the Makran mantle wedge (Al-Lazki et al., 2014) suggests that the degree of serpentinization is ~20%, in the range inferred for other subduction zones (e.g., Chou et al., 2009; Kamiya & Kobayashi, 2000; Ranero & Sallarès, 2004; Van Avendonk et al., 2011; Wada et al., 2008). Serpentinization of 15%–30% would reduce the density to ~3,000 kg m^{-3} (Hyndman & Peacock, 2003). The receiver functions indicate a nearly flat continental Moho across the region (Figure 6b); that is, there is no crustal root and the high topography region of the volcanic belt must be partially compensated by low densities (~3,150 kg m^{-3}) in the mantle, similar to that inferred for other subduction zones (Hyndman & Peacock, 2003). The high V_p/V_s ratio compared to that for 100% antigorite suggests that the low V_s we observe for the mantle wedge likely results from ~1%–2% partial melt of the mantle wedge, consistent with the petrochemistry of the Makran arc basalts (Saadat & Stern, 2011).

Data Availability Statement

Data analysis was performed primarily using Seismic Analysis Code (http://ds.iris.edu/ds/nodes/dmc/forms/sac/) (Goldstein et al., 2003) and Computer programs in seismology (http://www.eas.slu.edu/eqc/eqccps.html) (Herrmann, 2013), and plots were made using the Generic Mapping Tools (https://www.generic-mapping-tools.org/) (Wessel et al., 2019).

Acknowledgments
We thank Christian Haberland for providing a digital copy of his V_p model for the Makran Subduction Zone, Mohammad Tatar for teleseismic recordings from the INSN seismic network, Dan McKenzie for gravity data and James Jackson, Steven Roecker and Esmaeil Shabanian for helpful discussions. We also thank associate editor and two anonymous referees for their constructive comments which have helped us clarify our discussion. The receiver functions and surface wave data can be downloaded at https://data.mendeley.com/datasets/n38k-47whyv/1. This work was supported by the Royal Society under the International Collaboration Awards (ICA/R1/180234) and by NERC under the Earthquakes Without Frontiers project (NE/J019895/1) and by an IASBS internal grant. This is University of Cambridge, Earth Sciences publication esc.6037.

References

Abdetedal, M., Shomali, Z. H., & Gheitanchi, M. R. (2015). Ambient noise surface wave tomography of the Makran subduction zone, South-East Iran: Implications for crustal and uppermost mantle structures. *Earthquake Science*, *28*(4), 235–251. https://doi.org/10.1007/s11589-015-0132-1

Abdollahi, S., Ardestani, V. E., Zeyen, H., & Shomali, Z. H. (2018). Crustal and upper mantle structures of Makran subduction zone, SE Iran by combined surface wave velocity analysis and gravity modeling. *Tectonophysics*, *747*, 191–210. https://doi.org/10.1016/j.tecto.2018.10.005

Ahmadzadeh-Irandoust, M., Priestley, K., & Sobouti, F. (2022). Crustal structure of the Iranian plateau. to be submitted to Geochemistry, Geophysics, Geosystems. in preperation.

Al-Lazki, A. I., Al-Damegh, K. S., El-Hadidy, S. Y., Ghods, A., & Tatar, M. (2014). Pn-velocity structure beneath Arabia–Eurasia Zagros collision and Makran subduction zones. *Geological Society, London, Special Publications*, *392*(1), 45–60. https://doi.org/10.1144/sp392.3

Arthurton, R., Farah, A., & Ahmed, W. (1982). The Late Cretaceous-Cenozoic history of western Baluchistan Pakistan—The northern margin of the Makran subduction complex. *Geological Society, London, Special Publications*, *10*(1), 373–385. https://doi.org/10.1144/gsl.sp.1982.010.01.25

Audet, P., Bostock, M. G., Christensen, N. I., & Peacock, S. M. (2009). Seismic evidence for overpressured subducted oceanic crust and megathrust fault sealing. *Nature*, *457*(7225), 76–78. https://doi.org/10.1038/nature07650

Back, S., & Morley, C. K. (2016). Growth faults above shale–Seismic-scale outcrop analogues from the Makran foreland, SW Pakistan. *Marine and Petroleum Geology*, *70*, 144–162. https://doi.org/10.1016/j.marpetgeo.2015.11.008

Barnhart, W. D., Hayes, G. P., Samsonov, S. V., Fielding, E. J., & Seidman, L. E. (2014). Breaking the oceanic lithosphere of a subducting slab: The 2013 Khash, Iran earthquake. *Geophysical Research Letters*, *41*(1), 32–36. https://doi.org/10.1002/2013gl058096

Bensen, G., Ritzwoller, M., Barmin, M., Levshin, A., Lin, F., Moschetti, M., et al. (2007). Processing seismic ambient noise data to obtain reliable broad-band surface wave dispersion measurements. *Geophysical Journal International*, *169*(3), 1239–1260. https://doi.org/10.1111/j.1365-246x.2007.03374.x

Berberian, M., Jackson, J., Qorashi, M., Khatib, M., Priestley, K., Talebian, M., et al. (1999). The 1997 may 10 Zirkuh (Qa'enat) earthquake (M w 7.2): Faulting along the Sistan suture zone of eastern Iran. *Geophysical Journal International*, *136*(3), 671–694. https://doi.org/10.1046/j.1365-246x.1999.00762.x

Berberian, M., & King, G. (1981). Towards a paleogeography and tectonic evolution of Iran. *Canadian Journal of Earth Sciences*, *18*(2), 210–265. https://doi.org/10.1139/e81-019

Biabangard, H., & Moradian, A. (2008). Geology and geochemical evaluation of Taftan Volcano, Sistan and Baluchestan Province, southeast of Iran. *Chinese Journal of Geochemistry*, *27*(4), 356–369. https://doi.org/10.1007/s11631-008-0356-z

Bostock, M. (2013). The Moho in subduction zones. *Tectonophysics*, *609*, 547–557. https://doi.org/10.1016/j.tecto.2012.07.007

Bostock, M., Hyndman, R., Rondenay, S., & Peacock, S. (2002). An inverted continental Moho and serpentinization of the forearc mantle. *Nature*, *417*(6888), 536–538. https://doi.org/10.1038/417536a

Brocher, T. M. (2005). Empirical relations between elastic wavespeeds and density in the Earth's crust. *Bulletin of the Seismological Society of America*, *95*(6), 2081–2092. https://doi.org/10.1785/0120050077

Bröcker, M., Rad, G. F., Burgess, R., Theunissen, S., Paderin, I., Rodionov, N., et al. (2013). New age constraints for the geodynamic evolution of the Sistan Suture Zone, eastern Iran. *Lithos*, *170*, 17–34. https://doi.org/10.1016/j.lithos.2013.02.012

Burdick, L. J., & Langston, C. A. (1977). Modeling crustal structure through the use of converted phases in teleseismic body-wave forms. *Bulletin of the Seismological Society of America*, *67*(3), 677–691. https://doi.org/10.1785/bssa0670030677

Burg, J.-P. (2018). Geology of the onshore Makran accretionary wedge: Synthesis and tectonic interpretation. *Earth-Science Reviews*, *185*, 1210–1231. https://doi.org/10.1016/j.earscirev.2018.09.011

Byrne, D. E., Sykes, L. R., & Davis, D. M. (1992). Great thrust earthquakes and aseismic slip along the plate boundary of the Makran subduction zone. *Journal of Geophysical Research*, *97*(B1), 449–478. https://doi.org/10.1029/91jb02165

Camp, V., & Griffis, R. (1982). Character, genesis and tectonic setting of igneous rocks in the Sistan suture zone, eastern Iran. *Lithos*, *15*(3), 221–239. https://doi.org/10.1016/0024-4937(82)90014-7

Cawood, P. A., Kröner, A., Collins, W. J., Kusky, T. M., Mooney, W. D., & Windley, B. F. (2009). Accretionary orogens through Earth history. *Geological Society, London, Special Publications*, *318*(1), 1–36. https://doi.org/10.1144/sp318.1

Chai, C., Ammon, C. J., Maceira, M., & Herrmann, R. B. (2015). Inverting interpolated receiver functions with surface wave dispersion and gravity: Application to the western US and adjacent Canada and Mexico. *Geophysical Research Letters*, *42*(11), 4359–4366. https://doi.org/10.1002/2015gl063733

Chou, H.-C., Kuo, B.-Y., Chiao, L.-Y., Zhao, D., & Hung, S.-H. (2009). Tomography of the westernmost Ryukyu subduction zone and the serpentinization of the fore-arc mantle. *Journal of Geophysical Research*, *114*(B12). https://doi.org/10.1029/2008jb006192

Christensen, N. I. (1972). The abundance of serpentinites in the oceanic crust. *The Journal of Geology*, *80*(6), 709–719. https://doi.org/10.1086/627796

Christensen, N. I. (1996). Poisson's ratio and crustal seismology. *Journal of Geophysical Research*, *101*(B2), 3139–3156. https://doi.org/10.1029/95jb03446

Christensen, N. I. (2004). Serpentinites, peridotites, and seismology. *International Geology Review*, *46*(9), 795–816. https://doi.org/10.2747/0020-6814.46.9.795

Christensen, N. I., & Mooney, W. D. (1995). Seismic velocity structure and composition of the continental crust: A global view. *Journal of Geophysical Research*, *100*(B6), 9761–9788. https://doi.org/10.1029/95jb00259

Contreras-Reyes, E., Grevemeyer, I., Watts, A. B., Flueh, E. R., Peirce, C., Moeller, S., et al. (2011). Deep seismic structure of the Tonga subduction zone: Implications for mantle hydration, tectonic erosion, and arc magmatism. *Journal of Geophysical Research*, *116*(B10). https://doi.org/10.1029/2011jb008434

Contreras-Reyes, E., Ruiz, J. A., Becerra, J., Kopp, H., Reichert, C., Maksymowicz, A., et al. (2015). Structure and tectonics of the central Chilean margin (31°33°S): Implications for subduction erosion and shallow crustal seismicity. *Geophysical Journal International*, *203*(2), 776–791. https://doi.org/10.1093/gji/ggv309

Debayle, E., & Sambridge, M. (2004). Inversion of massive surface wave data sets: Model construction and resolution assessment. *Journal of Geophysical Research*. (B2), 109. https://doi.org/10.1029/2003jb002652

DeMets, C., Gordon, R. G., Argus, D., & Stein, S. (1990). Current plate motions. *Geophysical Journal International*, *101*(2), 425–478. https://doi.org/10.1111/j.1365-246x.1990.tb06579.x

Dolati, A., & Burg, J.-P. (2013). Preliminary fault analysis and paleostress evolution in the Makran Fold-and-Thrust Belt in Iran. In *Lithosphere dynamics and sedimentary basins: The Arabian plate and analogues* (pp. 261–277). Springer. https://doi.org/10.1007/978-3-642-30609-9_13

Dykstra, J. D., & Birnie, R. W. (1979). Reconnaissance geologic mapping in Chagai Hills, Baluchistan, Pakistan, by computer processing of Landsat data. *AAPG Bulletin*, *63*(9), 1490–1503. https://doi.org/10.1306/2f9185cc-16ce-11d7-8645000102c1865d

Dziewonski, A., Bloch, S., & Landisman, M. (1969). A technique for the analysis of transient seismic signals. *Bulletin of the Seismological Society of America*, *59*(1), 427–444. https://doi.org/10.1785/bssa0590010427

Eberhart-Phillips, D., Reyners, M., Chadwick, M., & Chiu, J.-M. (2005). Crustal heterogeneity and subduction processes: 3-D Vp, Vp/Vs and Q in the southern North Island, New Zealand. *Geophysical Journal International*, *162*(1), 270–288. https://doi.org/10.1111/j.1365-246x.2005.02530.x

Ellouz-Zimmermann, N., Deville, E., Müller, C., Lallemant, S., Subhani, A., & Tabreez, A. (2007). Impact of sedimentation on convergent margin tectonics: Example of the Makran accretionary prism (Pakistan). In *Thrust belts and foreland basins* (pp. 327–350). Springer. https://doi.org/10.1007/978-3-540-69426-7_17

Ellouz-Zimmermann, N., Lallemant, S., Castilla, R., Mouchot, N., Leturmy, P., Battani, A., et al. (2007). Offshore frontal part of the Makran Accretionary prism: The Chamak survey (Pakistan). In *Thrust belts and foreland basins* (pp. 351–366). Springer. https://doi.org/10.1007/978-3-540-69426-7_18

Engdahl, E. R., Jackson, J. A., Myers, S. C., Bergman, E. A., & Priestley, K. (2006). Relocation and assessment of seismicity in the Iran region. *Geophysical Journal International*, *167*(2), 761–778. https://doi.org/10.1111/j.1365-246x.2006.03127.x

Farhoudi, G., & Karig, D. (1977). Makran of Iran and Pakistan as an active arc system. *Geology*, *5*(11), 664–668. https://doi.org/10.1130/0091-7613(1977)5<664:moiapa>2.0.co;2

Ferris, A., Abers, G. A., Christensen, D. H., & Veenstra, E. (2003). High resolution image of the subducted Pacific (?) plate beneath central Alaska, 50–150 km depth. *Earth and Planetary Science Letters*, *214*(3–4), 575–588. https://doi.org/10.1016/s0012-821x(03)00403-5

Fowler, S. R., White, R. S., & Louden, K. E. (1985). Sediment dewatering in the Makran accretionary prism. *Earth and Planetary Science Letters*, *75*(4), 427–438. https://doi.org/10.1016/0012-821x(85)90186-4

Fruehn, J., White, R., & Minshull, T. (1997). Internal deformation and compaction of the Makran accretionary wedge. *Terra Nova*, *9*(3), 101–104. https://doi.org/10.1046/j.1365-3121.1997.d01-13.x

Fukao, Y., Hori, S., & Ukawa, M. (1983). A seismological constraint on the depth of basalt–eclogite transition in a subducting oceanic crust. *Nature*, *303*(5916), 413–415. https://doi.org/10.1038/303413a0

Gaedicke, C., Schlüter, H.-U., Roeser, H. A., Prexl, A., Schreckenberger, B., Meyer, H., et al. (2002). Origin of the northern Indus Fan and Murray Ridge, Northern Arabian Sea: Interpretation from seismic and magnetic imaging. *Tectonophysics*, *355*(1–4), 127–143. https://doi.org/10.1016/s0040-1951(02)00137-3

Ghazi, A., Hassanipak, A., Mahoney, J., & Duncan, R. (2004). Geochemical characteristics, 40Ar–39Ar ages and original tectonic setting of the Band-e-Zeyarat/Dar Anar ophiolite, Makran accretionary prism, SE Iran. *Tectonophysics*, *393*(1–4), 175–196. https://doi.org/10.1016/j.tecto.2004.07.035

Gholamzadeh, A., Yamini-Fard, F., Hessami, K., & Tatar, M. (2009). The February 28, 2006 Tiab earthquake, Mw 6.0: Implications for tectonics of the transition between the Zagros continental collision and the Makran subduction zone. *Journal of Geodynamics*, *47*(5), 280–287. https://doi.org/10.1016/j.jog.2009.01.005

Gilligan, A., & Priestley, K. (2018). Lateral variations in the crustal structure of the Indo–Eurasian collision zone. *Geophysical Journal International*, *214*(2), 975–989. https://doi.org/10.1093/gji/ggy172

Global Volcanism Program. (2020). *Bulletin of the global volcanism network (BGVN)*. Retrieved from https://volcano.si.edu/

Goldstein, P., Dodge, D., Firpoand, M., & Lee Minner, S. (2003). Signal processing and analysis tools for seismologists and engineers, 2003. In W. H. K. Lee, H. Kanamori, P. C. Jennings, & C. Kisslinger (Eds.), *Invited contribution to "The IASPEI International handbook of earthquake and engineering seismology"* (Vol. 81, pp. 1613–1620), Academic Press.

Grando, G., & McClay, K. (2007). Morphotectonics domains and structural styles in the Makran accretionary prism, offshore Iran. *Sedimentary Geology*, *196*(1–4), 157–179. https://doi.org/10.1016/j.sedgeo.2006.05.030

Grevemeyer, I., Ranero, C. R., Flueh, E. R., Kläschen, D., & Bialas, J. (2007). Passive and active seismological study of bending-related faulting and mantle serpentinization at the Middle America trench. *Earth and Planetary Science Letters*, *258*(3–4), 528–542. https://doi.org/10.1016/j.epsl.2007.04.013

Grevemeyer, I., Ranero, C. R., & Ivandic, M. (2018). Structure of oceanic crust and serpentinization at subduction trenches. *Geosphere*, *14*(2), 395–418. https://doi.org/10.1130/ges01537.1

Haberland, C., Mokhtari, M., Babaei, H. A., Ryberg, T., Masoodi, M., Partabian, A., et al. (2021). Anatomy of a crustal-scale accretionary complex: Insights from deep seismic sounding of the onshore western Makran subduction zone, Iran. *Geology*, *49*(1), 3–7. https://doi.org/10.1130/g47700.1

Haghipour, N., & Burg, J.-P. (2014). Geomorphological analysis of the drainage system on the growing Makran accretionary wedge. *Geomorphology*, *209*, 111–132. https://doi.org/10.1016/j.geomorph.2013.11.030

Haghipour, N., Burg, J.-P., Ivy-Ochs, S., Hajdas, I., Kubik, P., & Christl, M. (2015). Correlation of fluvial terraces and temporal steady-state incision on the onshore Makran accretionary wedge in southeastern Iran: Insight from channel profiles and 10Be exposure dating of strath terraces. *Bulletin*, *127*(3–4), 560–583. https://doi.org/10.1130/b31048.1

Hammond, W. C., & Humphreys, E. D. (2000). Upper mantle seismic wave velocity: Effects of realistic partial melt geometries. *Journal of Geophysical Research*, *105*(B510975–10), 986. https://doi.org/10.1029/2000jb900041

Herrmann, R. B. (2013). Computer programs in seismology: An evolving tool for instruction and research. *Seismological Research Letters*, *84*(6), 1081–1088. https://doi.org/10.1785/0220110096

Hoffmann, G., Rupprechter, M., Balushi, N. A., Grützner, C., & Reicherter, K. (2013). The impact of the 1945 Makran tsunami along the coastlines of the Arabian Sea (Northern Indian Ocean)–a review. *Zeitschrift für Geomorphologie*, *57*(Supplementary Issues 4), 257–277. https://doi.org/10.1127/0372-8854/2013/s-00134

Husen, S., Quintero, R., Kissling, E., & Hacker, B. (2003). Subduction-zone structure and magmatic processes beneath Costa Rica constrained by local earthquake tomography and petrological modelling. *Geophysical Journal International*, *155*(1), 11–32. https://doi.org/10.1046/j.1365-246x.2003.01984.x

Hutchison, I., Louden, K., White, R., & Von Herzen, R. (1981). Heat flow and age of the Gulf of Oman. *Earth and Planetary Science Letters*, *56*, 252–262. https://doi.org/10.1016/0012-821x(81)90132-1

Hyndman, R. D., & Peacock, S. M. (2003). Serpentinization of the forearc mantle. *Earth and Planetary Science Letters*, *212*(3–4), 417–432. https://doi.org/10.1016/s0012-821x(03)00263-2

Irandoust, M. A. (2021). *A seismic investigation of the crustal and uppermost mantle structure of the Iranian Platea. Ph.D. thesis*. Institute for Advanced Studies in Basic Sciences, Iran.

Ivandic, M., Grevemeyer, I., Berhorst, A., Flueh, E. R., & McIntosh, K. (2008). Impact of bending related faulting on the seismic properties of the incoming oceanic plate offshore of Nicaragua. *Journal of Geophysical Research*, *113*(B5). https://doi.org/10.1029/2007jb005291

Jackson, J., & MKenzie, D. (1984). Active tectonics of the Alpine—Himalayan Belt between western Turkey and Pakistan. *Geophysical Journal International*, *77*(1), 185–264. https://doi.org/10.1111/j.1365-246x.1984.tb01931.x

Jacob, K. H., & Quittmeyer, R. L. (1979). The Makran region of Pakistan and Iran: Trench-arc system with active plate subduction. *Geodynamics of Pakistan*, *305*, 317.

Ji, S., Li, A., Wang, Q., Long, C., Wang, H., Marcotte, D., et al. (2013). Seismic velocities, anisotropy, and shear-wave splitting of antigorite serpentinites and tectonic implications for subduction zones. *Journal of Geophysical Research*, *118*(3), 1015–1037. https://doi.org/10.1002/jgrb.50110

Kamiya, S., & Kobayashi, Y. (2000). Seismological evidence for the existence of serpentinized wedge mantle. *Geophysical Research Letters*, *27*(6), 819–822. https://doi.org/10.1029/1999gl011080

Kennett, B. L., Engdahl, E., & Buland, R. (1995). Constraints on seismic velocities in the Earth from traveltimes. *Geophysical Journal International*, *122*(1), 108–124. https://doi.org/10.1111/j.1365-246x.1995.tb03540.x

Khorrami, F., Vernant, P., Masson, F., Nilfouroushan, F., Mousavi, Z., Nankali, H., et al. (2019). An up-to-date crustal deformation map of Iran using integrated campaign-mode and permanent GPS velocities. *Geophysical Journal International*, *217*(2), 832–843. https://doi.org/10.1093/gji/ggz045

Kopp, C., Fruehn, J., Flueh, E., Reichert, C., Kukowski, N., Bialas, J., et al. (2000). Structure of the Makran subduction zone from wide-angle and reflection seismic data. *Tectonophysics*, *329*(1–4), 171–191. https://doi.org/10.1016/s0040-1951(00)00195-5

Kukowski, N., Schillhorn, T., Huhn, K., von Rad, U., Husen, S., & Flueh, E. R. (2001). Morphotectonics and mechanics of the central Makran accretionary wedge off Pakistan. *Marine Geology*, *173*(1–4), 1–19. https://doi.org/10.1016/s0025-3227(00)00167-5

Kuwatani, T., Okamoto, A., & Toriumi, M. (2011). Thermodynamic forward modeling of progressive dehydration reactions during subduction of oceanic crust under greenschist facies conditions. *Earth and Planetary Science Letters*, *307*(1–2), 9–18. https://doi.org/10.1016/j.epsl.2011.01.027

Langston, C. A. (1977). The effect of planar dipping structure on source and receiver responses for constant ray parameter. *Bulletin of the Seismological Society of America*, *67*(4), 1029–1050. https://doi.org/10.1785/bssa0670030713

Ligorria, J. P., & Ammon, C. J. (1999). Iterative deconvolution and receiver-function estimation. *Bulletin of the Seismological Society of America*, *89*(5), 1395–1400. https://doi.org/10.1785/bssa0890051395

Maekawa, H., Shozui, M., Ishll, T., Fryer, P., & Pearce, J. A. (1993). Blueschist metamorphism in an active subduction zone. *Nature*, *364*(6437), 520–523. https://doi.org/10.1038/364520a0

McCall, G. (1997). The geotectonic history of the Makran and adjacent areas of southern Iran. *Journal of Asian Earth Sciences*, *15*(6), 517–531. https://doi.org/10.1016/s0743-9547(97)00032-9

McCall, G., & Kidd, R. (1982). The Makran, Southeastern Iran: The anatomy of a convergent plate margin active from Cretaceous to Present. *Geological Society, London, Special Publications*, *10*(1), 387–397. https://doi.org/10.1144/gsl.sp.1982.010.01.26

McKenzie, D., & Sclater, J. G. (1971). The evolution of the Indian Ocean since the Late Cretaceous. *Geophysical Journal International*, *24*(5), 437–528. https://doi.org/10.1111/j.1365-246x.1971.tb02190.x

Melosh, H., & Raefsky, A. (1980). The dynamical origin of subduction zone topography. *Geophysical Journal International*, *60*(3), 333–354. https://doi.org/10.1111/j.1365-246x.1980.tb04812.x

Mokhtarzadeh, R. (2022). *Study of lithosphere and upper mantle structure and seismic anisotropy in Makran subduction zone, Ph.D. thesis*. Institute for Advanced Studies in Basic Sciences.

Motaghi, K., Shabanian, E., & Nozad-Khalil, T. (2020). Deep structure of the western coast of the Makran subduction zone, SE Iran. *Tectonophysics*, *776*(228), 314. https://doi.org/10.1016/j.tecto.2019.228314

Negaresh, H. (2008). Mud volcanoes in Sistan and Baluchestan Provinces, Makran coast, Iran. *Bulletin of the Geological Society of Malaysia*. *54*(54).

Niazi, M., Shimamura, H., & Matsu'ura, M. (1980). Microearthquakes and crustal structure off the Makran coast of Iran. *Geophysical Research Letters*, *7*(5), 297–300. https://doi.org/10.1029/gl007i005p00297

Nicholson, T., Bostock, M., & Cassidy, J. (2005). New constraints on subduction zone structure in northern Cascadia. *Geophysical Journal International*, *161*(3), 849–859. https://doi.org/10.1111/j.1365-246x.2005.02605.x

Ohmi, S., & Hurukawa, N. (1996). Detection of the subducting crust of oceanic plates beneath the Kanto district, Japan. *Tectonophysics*, *261*(4), 249–276. https://doi.org/10.1016/0040-1951(95)00150-6

Owens, T. J., Crosson, R. S., & Hendrickson, M. A. (1988). Constraints on the subduction geometry beneath western Washington from broadband teleseismic waveform modeling. *Bulletin of the Seismological Society of America*, *78*(3), 1319–1334. https://doi.org/10.1785/bssa0780010096

Page, W. D., Alt, J. N., Cluff, L. S., & Plafker, G. (1979). Evidence for the recurrence of large-magnitude earthquakes along the Makran coast of Iran and Pakistan. *Tectonophysics*, *52*(1–4), 533–547. https://doi.org/10.1016/b978-0-444-41783-1.50081-7

Pang, K.-N., Chung, S.-L., Zarrinkoub, M. H., Chiu, H.-Y., & Li, X.-H. (2014). On the magmatic record of the Makran arc, southeastern Iran: Insights from zircon U-Pb geochronology and bulk-rock geochemistry. *Geochemistry, Geophysics, Geosystems*, *15*(6), 2151–2169. https://doi.org/10.1002/2014gc005262

Peacock, S. M. (1993). The importance of blueschist -> eclogite dehydration reactions in subducting oceanic crust. *Geological Society of America Bulletin*, *105*(5), 684–694. https://doi.org/10.1130/0016-7606(1993)105<0684:tiobed>2.3.co;2

Peacock, S. M. (1996). Thermal and petrologic structure of subduction zones. In G. E. Bebout, D. W. Scholl, S. H. Kirby, J. P. Platt (Eds.), *Subduction*, (Vol. 96, pp. 119–133).

Peacock, S. M., & Wang, K. (1999). Seismic consequences of warm versus cool subduction metamorphism: Examples from southwest and northeast Japan. *Science*, *286*(5441), 937–939. https://doi.org/10.1126/science.286.5441.937

Penney, C., Copley, A., & Oveisi, B. (2015). Subduction tractions and vertical axis rotations in the Zagros–Makran transition zone, SE Iran: The 2013 May 11 M w 6.1 Minab earthquake. *Geophysical Journal International*, *202*(2), 1122–1136. https://doi.org/10.1093/gji/ggv202

Penney, C., Tavakoli, F., Saadat, A., Nankali, H. R., Sedighi, M., Khorrami, F., et al. (2017). Megathrust and accretionary wedge properties and behaviour in the Makran subduction zone. *Geophysical Journal International*, *209*(3), 1800–1830. https://doi.org/10.1093/gji/ggx126

Phinney, R. A. (1964). Structure of the Earth's crust from spectral behavior of long-period body waves. *Journal of Geophysical Research*, *69*(14), 2997–3017. https://doi.org/10.1029/jz069i014p02997

Platt, J., Leggett, J., Young, J., Raza, H., & Alam, S. (1985). Large-scale sediment underplating in the Makran accretionary prism, southwest Pakistan. *Geology*, *13*(7), 507–511. https://doi.org/10.1130/0091-7613(1985)13<507:lsuitm>2.0.co;2

Platt, J. P., Leggett, J. K., & Alam, S. (1988). Slip vectors and fault mechanics in the Makran accretionary wedge, southwest Pakistan. *Journal of Geophysical Research*, *93*(B7), 7955–7973. https://doi.org/10.1029/jb093ib07p07955

Ranero, C. R., & Sallarès, V. (2004). Geophysical evidence for hydration of the crust and mantle of the Nazca plate during bending at the north Chile trench. *Geology*, *32*(7), 549–552. https://doi.org/10.1130/g20379.1

Reynard, B. (2013). Serpentine in active subduction zones. *Lithos*, *178*, 171–185. https://doi.org/10.1016/j.lithos.2012.10.012

Reyss, J., Pirazzoli, P., Haghipour, A., Hatte, C., & Fontugne, M. (1999). Quaternary marine terraces and tectonic uplift rates on the south coast of Iran. *Geological Society, London, Special Publications*, *146*(1), 225–237. https://doi.org/10.1144/gsl.sp.1999.146.01.13

Rondenay, S., Abers, G. A., & Van Keken, P. E. (2008). Seismic imaging of subduction zone metamorphism. *Geology*, *36*(4), 275–278. https://doi.org/10.1130/g24112a.1

Saadat, S., & Stern, C. R. (2011). Petrochemistry and genesis of olivine basalts from small monogenetic parasitic cones of Bazman stratovolcano, Makran arc, southeastern Iran. *Lithos*, *125*(1–2), 607–619. https://doi.org/10.1016/j.lithos.2011.03.014

Schmidt, M. W., & Poli, S. (1998). Experimentally based water budgets for dehydrating slabs and consequences for arc magma generation. *Earth and Planetary Science Letters*, *163*(1–4), 361–379. https://doi.org/10.1016/s0012-821x(98)00142-3

Seno, T., Zhao, D., Kobayashi, Y., & Nakamura, M. (2001). Dehydration of serpentinized slab mantle: Seismic evidence from southwest Japan. *Earth Planets and Space*, *53*(9), 861–871. https://doi.org/10.1186/bf03351683

Shad Manaman, N., Shomali, H., & Koyi, H. (2011). New constraints on upper-mantle S-velocity structure and crustal thickness of the Iranian plateau using partitioned waveform inversion. *Geophysical Journal International*, *184*(1), 247–267. https://doi.org/10.1111/j.1365-246x.2010.04822.x

Shahabpour, J. (2010). Tectonic implications of the geochemical data from the Makran igneous rocks in Iran. *Island Arc*, *19*(4), 676–689. https://doi.org/10.1111/j.1440-1738.2010.00723.x

Smith, G., McNeill, L., Henstock, T. J., & Bull, J. (2012). The structure and fault activity of the Makran accretionary prism. *Journal of Geophysical Research*, *117*(B7). https://doi.org/10.1029/2012jb009312

Snead, R. J. (2002). Uplifted marine terraces along the Makran coast of Pakistan and Iran. In *Himalaya to the sea* (pp. 225–246). Routledge.

Sodoudi, F., Kind, R., Hatzfeld, D., Priestley, K., Hanka, W., Wylegalla, K., et al. (2006). Lithospheric structure of the Aegean obtained from P and S receiver functions. *Journal of Geophysical Research*, *111*(B12). https://doi.org/10.1029/2005jb003932

Syracuse, E. M., & Abers, G. A. (2006). Global compilation of variations in slab depth beneath arc volcanoes and implications. *Geochemistry, Geophysics, Geosystems*, *7*(5). https://doi.org/10.1029/2005gc001045

Taghizadeh-Farahmand, F., Afsari, N., & Sodoudi, F. (2015). Crustal thickness of Iran inferred from converted waves. *Pure and Applied Geophysics*, *172*(2), 309–331. https://doi.org/10.1007/s00024-014-0901-0

Tirrul, R., Bell, I., Griffis, R., & Camp, V. (1983). The Sistan suture zone of eastern Iran. *Geological Society of America Bulletin*, *94*(1), 134–150. https://doi.org/10.1130/0016-7606(1983)94<134:tsszoe>2.0.co;2

Ulmer, P., & Trommsdorff, V. (1995). Serpentine stability to mantle depths and subduction-related magmatism. *Science*, *268*(5212), 858–861. https://doi.org/10.1126/science.268.5212.858

Van Avendonk, H. J., Holbrook, W. S., Lizarralde, D., & Denyer, P. (2011). Structure and serpentinization of the subducting Cocos plate offshore Nicaragua and Costa Rica. *Geochemistry, Geophysics, Geosystems*, *12*(6). https://doi.org/10.1029/2011gc003592

Van der Meer, D. G., Van Hinsbergen, D. J., & Spakman, W. (2018). Atlas of the underworld: Slab remnants in the mantle, their sinking history, and a new outlook on lower mantle viscosity. *Tectonophysics*, *723*, 309–448. https://doi.org/10.1016/j.tecto.2017.10.004

Vernant, P., Nilforoushan, F., Chery, J., Bayer, R., Djamour, Y., Masson, F., et al. (2004). Deciphering oblique shortening of central Alborz in Iran using geodetic data. *Earth and Planetary Science Letters*, *223*(1–2), 177–185. https://doi.org/10.1016/j.epsl.2004.04.017

Vernant, P., Nilforoushan, F., Hatzfeld, D., Abbassi, M., Vigny, C., Masson, F., et al. (2004). Present-day crustal deformation and plate kinematics in the Middle East constrained by GPS measurements in Iran and Northern Oman. *Geophysical Journal International*, *157*(1), 381–398. https://doi.org/10.1111/j.1365-246x.2004.02222.x

Von Rad, U., Berner, U., Delisle, G., Doose-Rolinski, H., Fechner, N., Linke, P., et al. (2000). Gas and fluid venting at the Makran accretionary wedge off Pakistan. *Geo-Marine Letters*, *20*(1), 10–19. https://doi.org/10.1007/s003670000033

Wada, I., Wang, K., He, J., & Hyndman, R. D. (2008). Weakening of the subduction interface and its effects on surface heat flow, slab dehydration, and mantle wedge serpentinization. *Journal of Geophysical Research*, *113*(B4). https://doi.org/10.1029/2007jb005190

Walker, R. T., Talebian, M., Saiffori, S., Sloan, R. A., Rasheedi, A., MacBean, N., et al. (2010). Active faulting, earthquakes, and restraining bend development near Kerman city in southeastern Iran. *Journal of Structural Geology*, *32*(8), 1046–1060. https://doi.org/10.1016/j.jsg.2010.06.012

Wessel, P., Luis, J., Uieda, L., Scharroo, R., Wobbe, F., Smith, W., et al. (2019). The generic mapping tools version 6. *Geochemistry, Geophysics, Geosystems*, *20*(11), 5556–5564. https://doi.org/10.1029/2019gc008515

Wiedicke, M., Neben, S., & Spiess, V. (2001). Mud volcanoes at the front of the Makran accretionary complex, Pakistan. *Marine Geology*, *172*(1–2), 57–73. https://doi.org/10.1016/s0025-3227(00)00127-4

Wilson, J. T. (1954). The development and structure of the crust. In G. P. Kuiper (Ed.), *The earth as a planet* (pp. 138–214). University of Chicago Press.

Wunder, B., & Schreyer, W. (1997). Antigorite: High-pressure stability in the system MgO-SiO_2-H_2O (MSH). *Lithos*, *41*(1–3), 213–227. https://doi.org/10.1016/s0024-4937(97)82013-0

Xia, S., Zhao, D., & Qiu, X. (2008). Tomographic evidence for the subducting oceanic crust and forearc mantle serpentinization under Kyushu, Japan. *Tectonophysics*, *449*(1–4), 85–96. https://doi.org/10.1016/j.tecto.2007.12.007

Yamini-Fard, F., Hatzfeld, D., Farahbod, A., Paul, A., & Mokhtari, M. (2007). The diffuse transition between the Zagros continental collision and the Makran oceanic subduction (Iran): Microearthquake seismicity and crustal structure. *Geophysical Journal International*, *170*(1), 182–194. https://doi.org/10.1111/j.1365-246x.2006.03232.x

Yuan, X., Sobolev, S. V., Kind, R., Oncken, O., Bock, G., Asch, G., et al. (2000). Subduction and collision processes in the Central Andes constrained by converted seismic phases. *Nature*, *408*(6815), 958–961. https://doi.org/10.1038/35050073